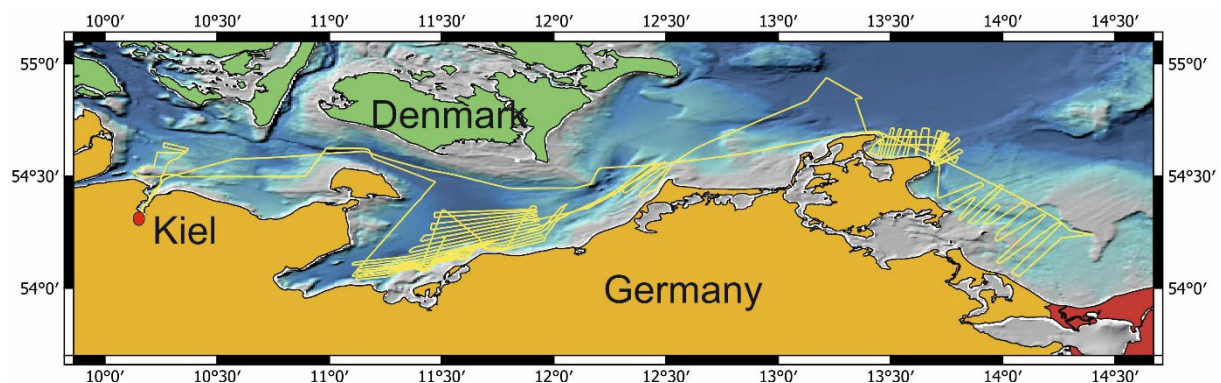ALKOR-Berichte

Studierendenbericht
Seepraktikum Geophysik 2022 (UHH)

Cruise No. AL582

04.10.2022 - 15.10.2022
Kiel (Germany) - Kiel (Germany)
Seepraktikum 22-UHH

Hübscher, C., Aykalaycı, T., Friedrich, A., Hampel, G., Ischebeck, L., Kristen, E., Oelkers, R., Warwel, A., Wintermeyer, A., Wünsch, M., Zwetzich, R.

Chief Scientist: Christian Hübscher
Universität Hamburg
2022

Table of Contents

1 Cruise Summary

1.1 Summary in English

(C. Hübscher)

The internship cruise AL582, in which a total of 9 students participated, started with the loading of the ship on October 4, 2022 at the GEOMAR pier in Kiel. With the rigging of the working deck and the laboratories, the instruction of the students in the various measuring instruments also began, which was further deepened in the following days at sea. The rather stormy weather influenced the work during the first days at sea. The scientific work program started with hydroacoustic and magnetic measurements in the Bay of Kiel before the transit to the Bay of Mecklenburg began. The goal of the seismic measurements here was to map the Middle Jurassic unconformity above a salt pillow. During the second half of the expedition, the aim was to map the glacial erosional unconformity around Jasmund. Above the erosional base, ice glaciers scraped Cretaceous deposits during the last cold period and pushed them together to form glaci-tectonic complexes. These complexes are known as the "chalk cliffs of Rügen". By the end of their time on board, students had gained in-depth knowledge of data acquisition, processing, and interpretation. Last but not least, the students learned what it means to work on a research vessel. The cruise ended in Kiel on October 15, 2022.

1.2 Zusammenfassung

(C. Hübscher)

Die Praktikumsfahrt AL582, an der insgesamt 9 Studierende teilnahmen, begann mit der Beladung des Schiffes am 4. Oktober 2022 an der GEOMAR Pier in Kiel. Mit dem Aufrüsten des Arbeitsdecks und der Labore begann auch die Einweisung der Studierenden in die verschiedenen Messgeräte, die in den folgenden Tagen auf See weiter vertieft wurde. Das insgesamt recht stürmische Wetter beeinflusste die Arbeiten in den ersten Tagen auf See. Begonnen wurde mit hydroakustischen und magnetischen Messungen in der Kieler Bucht, bevor der Transit in die Mecklenburger Bucht begann. Ziel der seismischen Messungen hier war die Kartierung der Mittel-Jurassischen Erosionsdiskordanz oberhalb eines Salzkissens. Während der zweiten Hälfte der Expedition war das Ziel die Kartierung der glazialen Erosionsdiskordanz rund um Jasmund. Oberhalb der Erosionsbasis haben während der letzten Kaltzeit Eisgletscher kreidezeitliche Ablagerungen abgeschabt und zu glazitektonischen Komplexen zusammengeschoben. Diese Komplexe sind als „Kreidefelsen von Rügen" bekannt. Am Ende ihrer Zeit an Bord hatten die Studierenden vertiefte Kenntnisse über die Datengewinnung, -bearbeitung und Interpretation gewonnen. Nicht zuletzt erfuhren die Studierenden, was es bedeutet, auf einem Forschungsschiff zu arbeiten. Die Ausfahrt endete am 15. Oktober 2022 in Kiel.

2.   Participants

2.1   Principal Investigators

Name	Institution
Hübscher, Christian, Prof. Dr.	IfG-HH

2.2   Scientific Party

Name	Discipline	Institution
Prof. Dr. Hübscher, Christian	Chief scientist	IfG-UHH
Aykalaycı, Tuğçe	Student	IfG-UHH
Friedrich, Annalena	Student	IfG-UHH
Hampel, Gina	Student	IfG-UHH
Ischebeck, Lisa	Student	IfG-UHH
Kristen, Elias	Student	IfG-UHH
Oelkers, Robert	Student	IfG-UHH
Warwel, Arne	Supervisor	IfG-UHH
Winter, Sven	Technician	IfG-UHH
Wintermeyer, Alina	Student	IfG-UHH
Wünsch, Moritz	Student	IfG-UHH
Zwetzich, Richard	Student	IfG-UHH

2.3   Participating Institutions

IfG-UHH   Institut für Geophysik, Universität Hamburg

3.   Research Programme

3.1   Description of the Work Area

(T. Aykalaycı)

The Central European Southern Permian Basin (SPB), shown in figure 3.1, is an intracontinental basin with a complex tectonostratigraphic history from the Carboniferous through the present and fragmented into subbasins and fault zones (Littke et al. 2008a; Warsitzka et al. 2019), for example the Gardelegen Fault (Schretzenmayr 1993; Kossow et al. 2000).
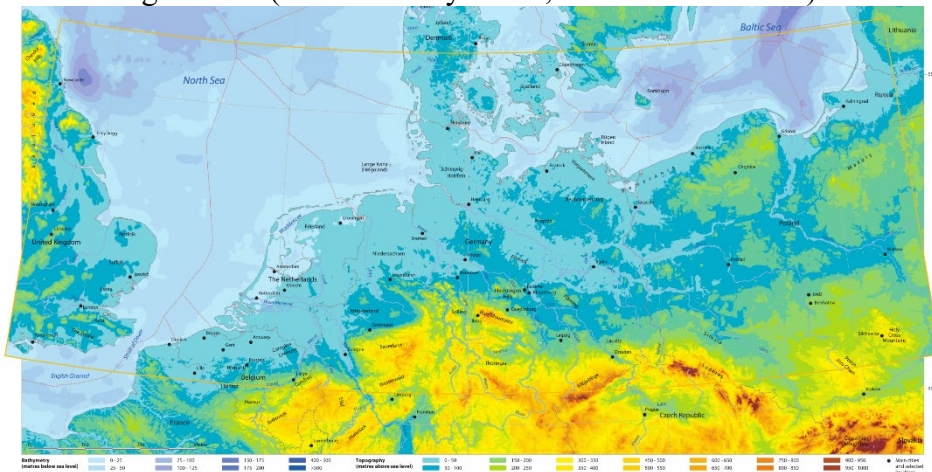
Fig. 3.1   Topography and bathymetry map (Petroleum Geological Atlas of the Southern Permian Basin Area, 2010).
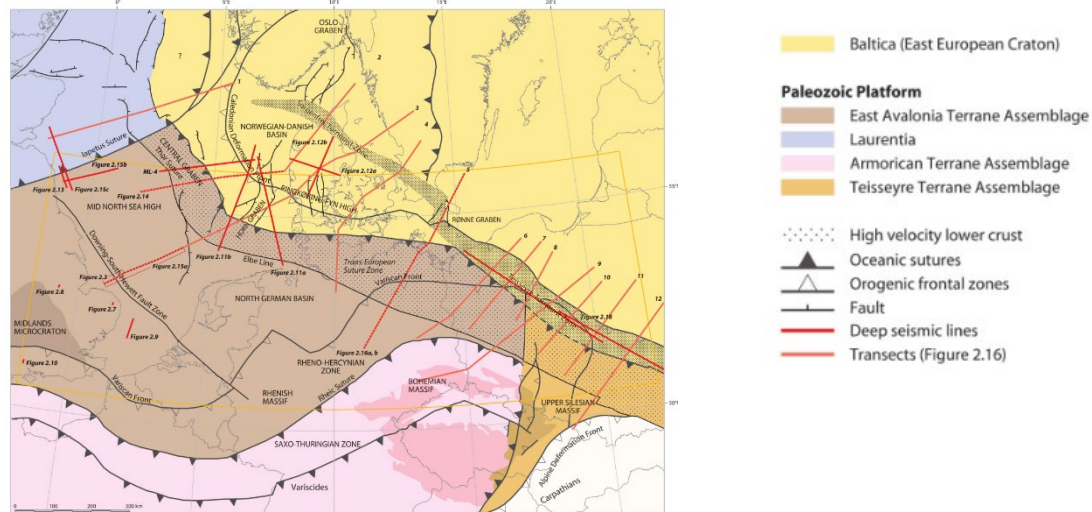
Fig. 3.2   Crustal structure of the Southern Permian Basin area and its surroundings. The main tectonic structures and lineaments are shown together with the locations of the main deep seismic lines (Petroleum Geological Atlas of the Southern Permian Basin Area, 2010).

The North German basin (NGB) is part of the Southern Permian Basin (Ziegler 1990; Marotta 2000), which extends from Britain over central Europe to Poland (Maystrenko et al. 2008; Ahlrichs et al. 2020). The basin has a complex polyphase history since the Carboniferous±Permian formation (Scheck et al. 1999; Marotta et al. 2000). In the latest Carboniferous-Permian, WNW-ESE extension and transtension has started its formation accompanied by the deposition of Carboniferous volcanics, coal, and Lower Permian volcanics and clastics (Bachmann et al. 2008; Maystrenko

et al. 2008; Ziegler 1990; Ahlrichs et al. 2020). The main tectonic structures are highlighted in Fig. 3.2.

Besides, multiphase deformation during the Caledonian and Variscan orogenies significantly affected the underlying basement rocks (Kossow et al. 2000; Krawczyk et al. 1999). In late Permian times, Zechstein layered evaporite sequence was deposited in response to a series of marine transgressions (Kossow and Krawczyk 2002) and clay, carbonates, anhydrite, halite and potash sequences in various quantities were formed because of repeated restricted seawater influx under arid conditions (Peryt et al., 2010; Ahlrichs et al. 2022; Strohmenger et al. 1996). During the complex polyphase formation, the Zechstein evaporite sequence caused the formation of various salt structures, including salt pillows, salt diapirs and salt walls, as can be seen in Fig. 3.3 (Ahlrichs et al. 2022).
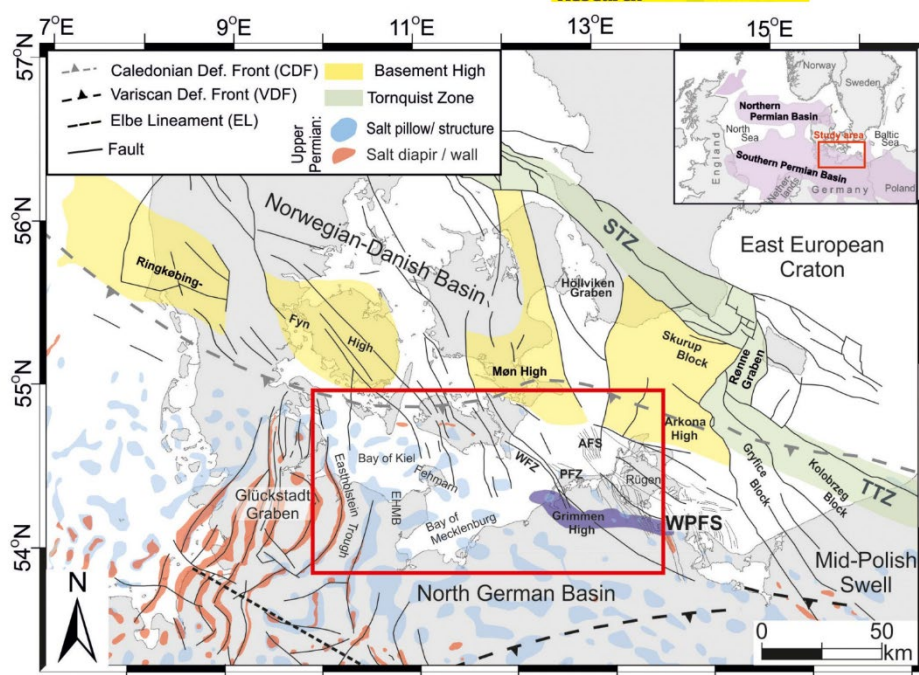
Fig. 3.3   Structural elements of the northern North German Basin (Ahlrichs et al. 2022).

This was followed by a period of thermal subsidence, which lasted until the Late Triassic (Scheck et al. 1999) and continued until Middle Triassic times (Scheck 1997; Kossow et al. 2000) which the Buntsandstein and Muschelkalk successions were deposited consisted of interlayered mudstones and carbonates (Ahlrichs et al. 2022). Then, at the center of the Glückstadt Graben, thermal collapse was interrupted by the formation of a constricted graben, in Early to Middle Triassic times (Brink et al., 1992).
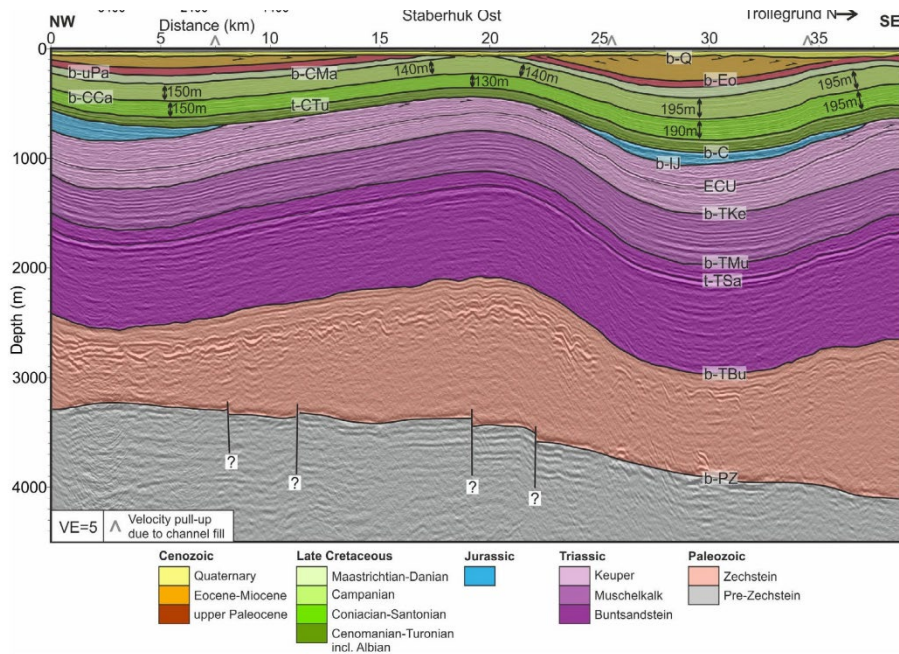
Fig. 3.4   Thermal doming in the study area (Ahlrichs et al. 2022).

Thermal doming, for example Fig. 3.4 occurred in the North Sea from the Middle Jurassic to the Late Jurassic, resulting in large-scale uplift and erosion of Jurassic and partially Triassic deposits in the NGB (Graversen, 2006; Ahlrichs et al. 2020). During the Late Cretaceous times, the overall stress regime is changed because of NW-SE to N-S directed shortening to compressive. Then, compressive stress caused normal faults to turn into reverse faulting as well as the initiation and folding of reverse faults. Additional pulses of uplift and inversion with the development of E-W to NW-SE oriented extension continued in the Early Paleocene and Late Eocene (Bachmann et al., 2010; Maystrenko et al. 2008; Ahlrichs et al. 2020).

Development resumed from Late Cretaceous to Albian and continued with a relatively calm tectonic phase from Cenomanian to Turonian in which long-term horizontal bedded chalk units were deposited in shallow and deep sea conditions (Kossow Krawczyk, 2002; Vejbaek at all., 2010; Ahlrichs, 2022).

3.1.1   The Baltic Sector of the North German Basin

(T. Aykalaycı)

The Baltic Sea sector of the NGB, shown in Figure 3.5, stretches from the Bay of Kiel in the west to Rügen Island in the east. NGB depocenter with up to 11 km of post-Permian sediment thickness is formed by Eastholstein. Through marking the part of the NNE–SSW trending Mesozoic–Cenozoic Glückstadt Graben, which is covered by the western Bay of Kiel (Maystrenko et al., 2005b).
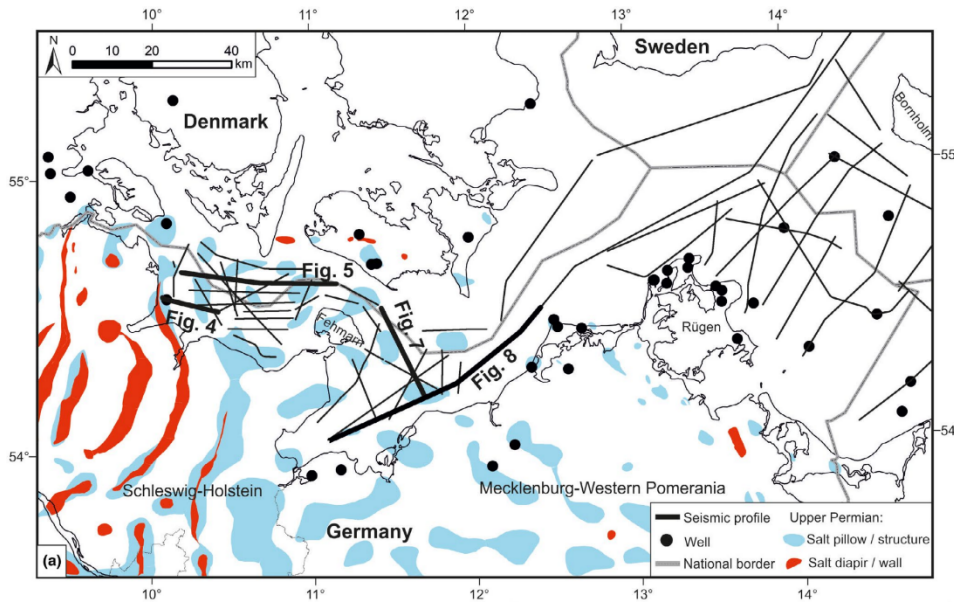
Fig. 3.5   Maps showing the location of seismic profiles and wells in North German Basin (Ahlrichs et al. 2022).

The western Kiel Bay includes the Eastholstein Trench, which marks the part of the NSW-SSW trending Mesozoic-Cenozoic Glückstadt Graben, which forms an NGB deposition center with a post Permian sediment thickness of 11 km, while the Eastholstein Mecklenburg Block shown in Fig. 3.6 , the peripheral zone between the Glückstadt Graben and the north watershed edge towards Rügen Island, is covered by the central to Bay of Kiel and the Bay of Mecklenburg Glückstadt Graben (Maystrenko et al., 2005b).
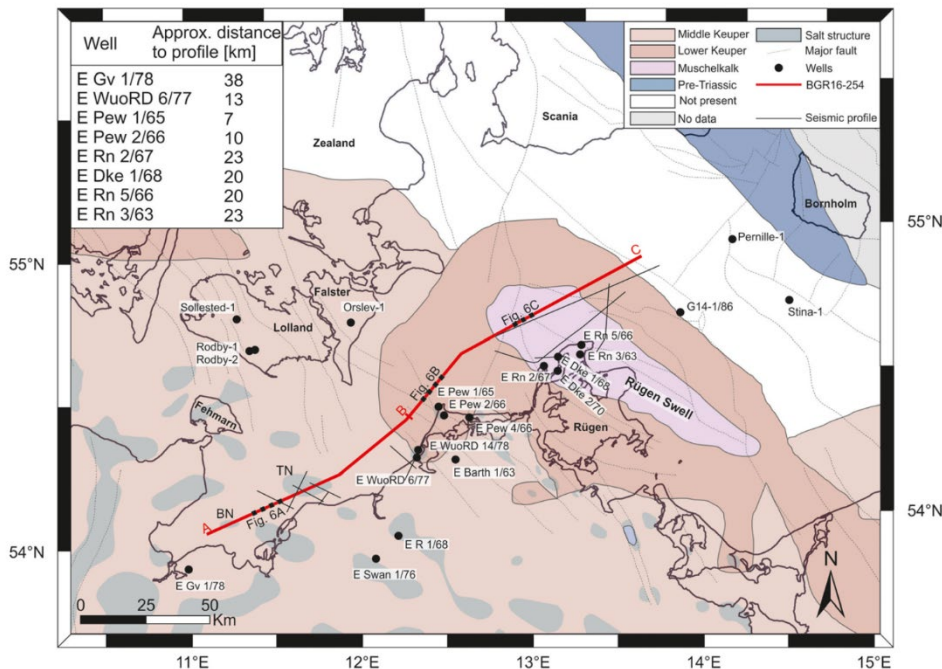
Fig. 3.6   Subcrop map of the Early Cimmerian Unconformity (Ahlrichs et al. 2020).

After precipitation in the Turonian, compression stress is transmitted to the European foreland due to the onset of the African-Iberian-European convergence and the massive remodeling of grand plate (Kley Voigt, 2008). Then, uplift, erosion, and renewed salt movement arose as a result of

horizontal shortening at the northern NSW border emerged (Hansen et al., 2007; Hübscher et al., 2010; Kossow Krawczyk, 2002).

Erosion is increasing westward from the Bay of Mecklenburg and Hübscher et al. (2010) and Al Hseinat and Hübscher (2017) attribute this to the Central North Sea doming event, as can be seen in Fig. 3.7 (Graversen, 2006; Underhill Partington, 1993; Ziegler, 1990). Sea level rise, which remained high until the Campanian, first caused a major rupture and then the resumption of sedimentation (Vejbaek et al., 2010), and while this went on until early Turonian times, also it marked a period of relative tectonic stagnation (Kossow Krawczyk, 2002; Scheck Bayer, 1999; Vejbaek et al., 2010).
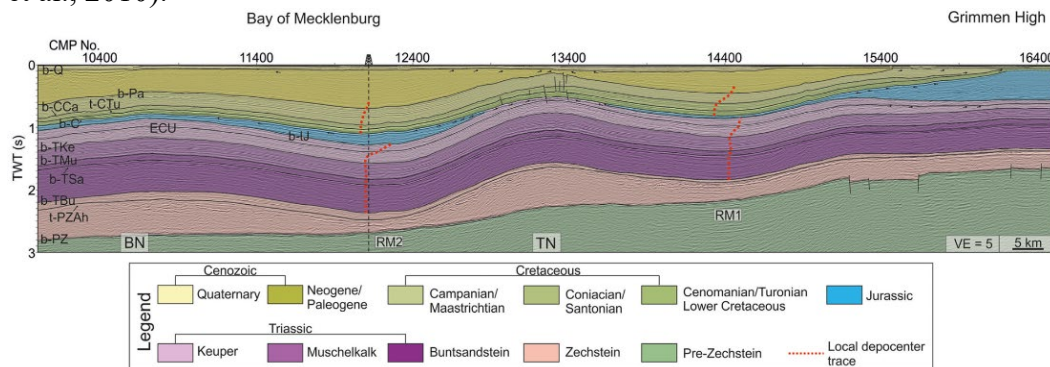
**Fig. 3.7**   Time migrated and interpreted section. F= fault; PR = Prerow salt pillow (Ahlrichs et al. 2020).

Due to the realignment of the grand plates, the onset of African-Iberian-European convergence, and the Pyrenees and Alpine orogeny, the Baltic Sea sector has undergone several uplift and reversal pulses from Santonian to Cenozoic (Kley, 2018; Kley Voigt, 2008). Horizontal shortening, reversal impact, from the Late Turonian/Santonian to the Maastrichtian reactivated pre-existing basement faults that led to uplift and erosion at the north basin margin (Kley, 2018; Kley Voigt, 2008; Kossow Krawczyk, 2002).

The uplift of the Grimmen High, which began in the Coniacian towards the Santonian and culminated in the Campanian Maastrichtian, caused only slight reversal of the Glückstadt Graben, indicated by the slight uplift of the diapir roofs and little salt movement at the edges of the graben. (Maystrenko et al., 2005b, 2006). Reversal induced elevations throughout the Tornquist Zone influenced depositional patterns in the Chalk Sea through contour currents were generated because of the inversion (Hübscher et al., 2019; and references therein). Tuft of moving Zechstein salt northeast of Grimmen High resulted in increased resistance to northward spreading overload deformation that resulted in the uplift of Grimmen High (Kossow et al., 2000; Kossow Krawczyk, 2002).
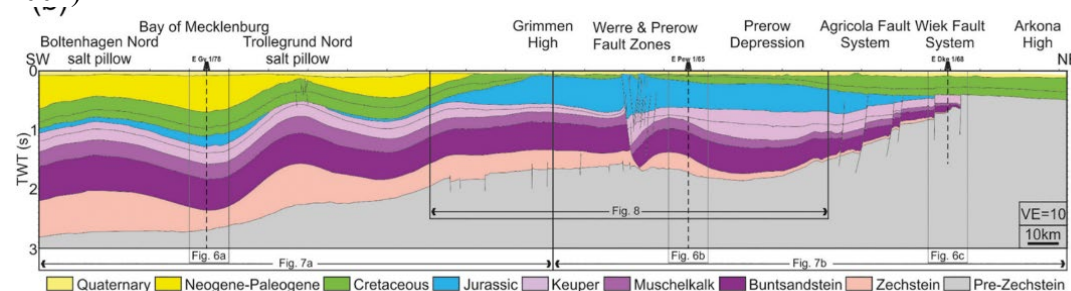
Fig. 3.8   Condensed geological cross section along profile analyzed North German Basin, showing main structures and stratigraphic features (Ahlrichs et al. 2020).

Cenozoic deposits on the salt pads in the Bay of Mecklenburg from the Late Cretaceous to the Cenozoic show a very strong decrease in thickness and increased salt pad growth (Fig. 3.8). In addition, during the Neogene a stress orientation change from NE-SW to NW-SE elongation resulted in reactivation of intensified salt movement and faulting (Al Hseinat and Hübscher, 2017; Hübscher et al., 2010; Kammann et al., 2016). Scandinavia is an elevated sediment source from Paleocene to Oligocene, with Paleogene conditions being between shallow and deep sea (Japsen et al., 2007; Nielsen et al., 2002). Upper Paleocene claystones, which are largely preserved west of Grimmen High, overlie the associated widespread unconformity (Vinken International Geological Correlation Programme, 1988). A relative tectonic stagnation phase is observed in the early and middle Eocene (Hinsch, 1986; Katzung, 2004).

In the Glückstadt Graben, the E-W directional widening is reactivated movement of salt with the thickest sediment deposition and salt retraction at the margins in late Eocene times (Maystrenko et al., 2005b). Reactivated Salt flow continued from late Eocene to Oligocene companioned faulting of the salt wall in the Eastholstein Trough in the western Bay of Kiel (Al Hseinat at al., 2016).

3.1.2 The Upper Weichselian Glaciotectonic Complex of Rügen

(E. Kristen)

The history of the island of Rügen is closely connected to the formation of the Baltic Sea. It is therefore important to retrace the development of the Baltic Sea throughout the last geological eras to understand how the remnants formed that can be explored today.

During the Perm period 270 million years ago, the predecessor of the Baltic basin lay was located 25° North. The consequence of the shift to a warmer climate at the end of this period left the region experiencing a subtropical - arid climate supporting evaporation. This led to the deposition of salt, which can be found particularly in the western region of the Baltic Sea and the North German Plain today (Fig. 3.3). During the Cretaceous era, which started 145 million years ago, the characteristic chalk layers formed, composed primarily out of marine shell material.
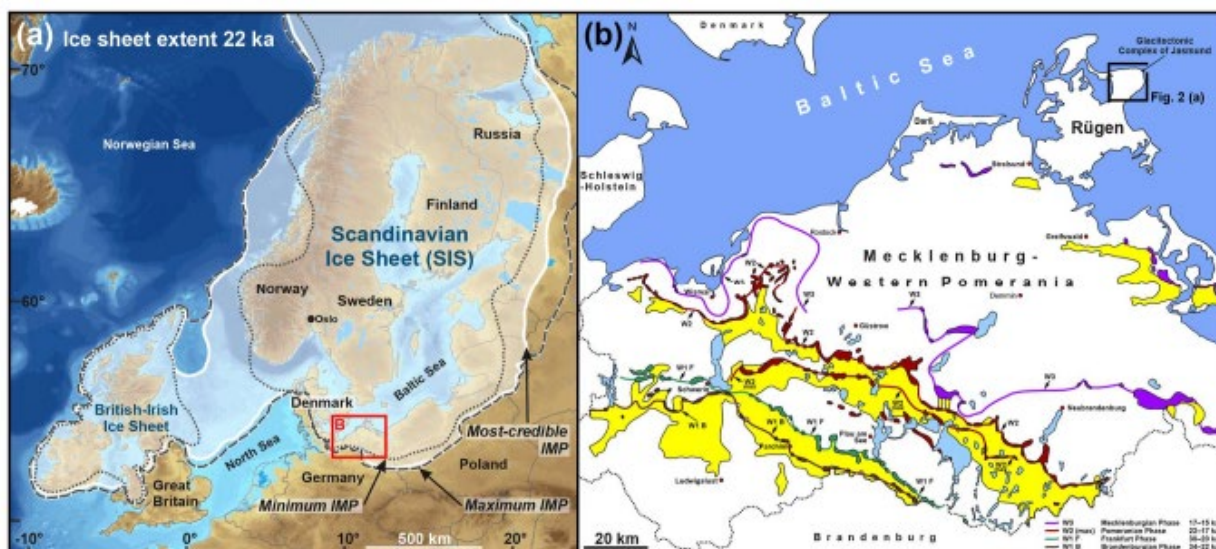

Fig. 3.9   Estimated extend of glaciers during the Weichselian Gleciation (Kenzler and Hüneke 2019)

During the last glacial period, the Weichselian Glaciation, till and sediment was pushed southwards by large glaciers spanning the northern part of the European continent. This material formed

typical structures as moraines and outliers. The estimated extend of the ice sheet can be seen in figure 3.9. During warmer periods, cretaceous deposits in specific areas were resurfaced due to post-glacial rebound and interaction with the alpine glaciers. During the final advance of the Weichselian Glaciation the glacial sheet pressed southwards. The following retreat left the characteristic fold-and thrust structures, described in the previous chapter. This marked the end of the Weichselian Glaciation and therefore the Pleistocene. The Holocene began.

The history of the Baltic Sea during the Holocene can be subdivided into four main stages. First, it existed as the Baltic Ice Lake, consisting of fresh water. Due to the continues retreat of the glaciers to the Scandinavian mountains, the eustatic sea level rose, resulting in a direct connection to the North Sea. Consequently, the water of the former Baltic Ice Lake turned to brackish water. In a third phase, the passage connection to the North Sea closed again as a result of the post-glacial uplifting of southern Scandinavia. As Scandinavia rose, the North German Plain subsided and paved the way for the – now again fresh – water and advanced to what is today Germanys coastline of the Baltic Sea. At last, the Baltic Lake regained a passage to the North Sea again due to global eustatic sea level rise, and the landscape formed by glacial processes were drown in a rapid water rise. This left these structures comparatively intact, as the typical erosion processes associated with a slow water rise did not occur. Rügen, one of the few regions at the German Baltic coast that experienced uplifting, withstood sinking into the Baltic Sea. This geological history explains what we see today at the chalk coast of the island Rügen (e.g. fig. 3.10). The cretaceous material experienced stress exerted by glaciers and is covered by Pleistocene deposits brought in by them.

Fig. 3.10   The geological setting of Rügen (Kenzler and Hüneke 2019)

3.1.3   Glacially Triggered Faulting

(A. Friedrich)

Approximately 20 000 years ago, the Baltic Sea was still captured by kilometres of a glacial ice sheet. In this report, we discuss a paper by Steffen et al. on glacially triggered faulting, where the effects of glacial cycles on the lithosphere, i.e. the stress profile and its capabilities in different faulting regimes, are analysed and classified.

The Earth's stress profile can be altered via various mechanisms, e. g. tectonic forces, sedimentation or erosion, but also glacial cycles, which consist of loading and unloading phases with an everchanging glacial mass profile. In addition to that, the removal of a glacier (deglaciation) is another cause of stress changes.

While the timescales for tectonic stresses lie on the order of a few mega years, glacial cycles can induce significant stress changes during just a few thousand years. Therefore, tectonic stresses are mostly assumed to be constant with respect to the effects of glacial cycles. While the induced stress changes by glaciers are usually not sufficient to trigger new fault creations, they have the ability to reactivate old faults, given the right circumstances.
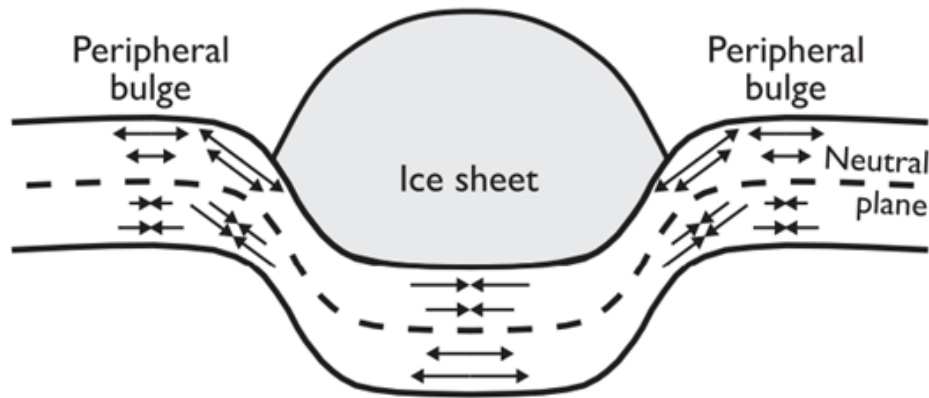
Fig. 3.11   Glacially induced bulging (Steffen et al. 2021)

Due to the typical morphology of glaciers, they exercise characteristic types of stress in different regions, able to reactivate or even stabilize different types of faults.

It makes sense to roughly divide the glacier into three regions: The peripheral bulge, which is an area away from the ice sheet (schematic drawing in Fig. 11); the 'transition area' between the peripheral bulge and the ice margin; and the central ice sheet area.

Faults are tectonic ruptures or fractures in the lithosphere where two rock surfaces are offset from each other. They can be distinguished by the angle with respect to a plane perpendicular to the surface, and the direction of the slip.

The three main types of stress regimes discussed by Steffen et al. are *thrust faults, normal faults,* and *strike-slip faults* (Fig. 3.12).
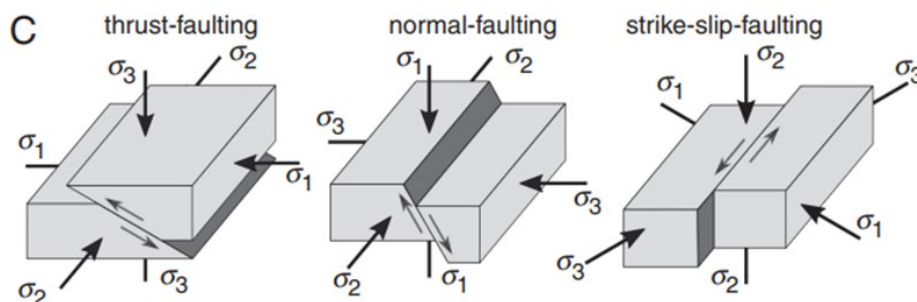
Fig. 3.12   Faulting mechanisms in stress regimes (Steffen et al. 2019)

They concluded that there are (in addition to site-dependent effects) three main components that matter with respect to fault reactivation: The location with respect to the glacier, the background stress regime, and the timing, where they distinguish glaciation, deglaciation, and long-term-effects for the latter.

On the one hand, deglaciation can lead to reactivation only of thrust-faulting stress regimes that lie beneath the central region of the glacier. On the other hand, the peripheral bulge regions of glaciers can destabilize normal-faulting or strike-faulting stress regimes even during the glaciation.

After deglaciation, these areas in these regimes remain unstable for a brief time but regain stability shortly after.

In the transitional area between peripheral bulge and ice margin, thrust-faulting stress regimes are destabilized during the glaciation due to compression effects.

Steffen et al. conclude that the glacial stress regimes have to be taken into account for conclusions on the stability of faults, and remark that the background stress regimes and differently aligned faults are affected in diverse ways, requiring further investigation on case-by-case bases.

3.1.4   Hydrocarbon Source Rock in the North German Basin

(T. Aykalaycı)

The North and South Permian Basins formed along the NW-SE and WNW-ESE trending axes with the subsequent connection of NGB depocenters (Ziegler 1990) and were separated by a parallel Mid North Sea-RFZ high chain. Besides, it contains Rotliegend which is thick series of clastic rocks overlain by the upper Permian Zechstein evaporites (Littke et al. 2008b). In the North Permian Basin, the thickness of the Rotliegend rarely exceeds 300 m (James et al. 2003; Lockhorst et al. 1998), whereas the South Permian Basin, which includes the South North Sea, the North German Basin (Bachmann and Hoffmann 1997; McCann 1999; Plein 1995; Scheck and Bayer 1999) and the Polish Basin, is the thickest Rotliegend in Central Europe up to 2300 m along the axis of the North German Basin and in the Polish Basin about 1600 m (Dadlez et al. 1995, 1998b; Kiersnowski et al. 1995; Lockhorst et al. 1998; ScheckWenderoth and Lamarche 2005, Littke et al. 2008b).
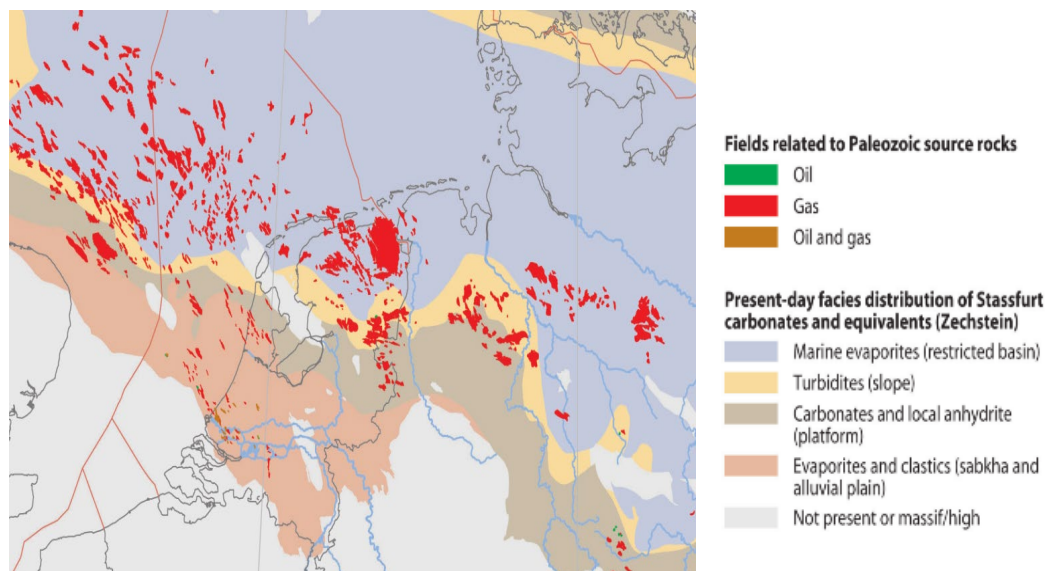
Fig. 3.13   The petroleum provinces and districts in the North German Basin (Petroleum Geological Atlas of the Southern Permian Basin Area, 2010).

The collapses analysed as a result of the studies so far (Wees et al. 2000; Littke et al. 2008b) are as follows: In the Southern Permian Basin, Late Carboniferous – Early Permian crustal expansion followed by delayed filling and thermal collapse took place. The thinner Rotliegend sequence in the North Permian Basin documents the onset of a later post-rift thermal subsidence than in the

South Permian Basin (Littke et al. 2008b). During the late Permian Zechstein time, significant post-rift subsidence was observed in the North Permian Basin (Vejbaek 1997, Littke et al. 2008b). The Late Carboniferous includes the most important gas source rocks, coal-bearing strata, in the basin (Littke et al. 2008b). When examining the Rotliegend deposits which include important gas reservoir sandstones, as can be seen in Fig. 3.13, they were deposited only in the Central Netherlands Basin (CNB) during that time (Littke et al. 2008b).

The Mittelplate (Fig. 3.14) field is the largest oil field in Germany, and thus several exploration and production wells have been drilled in this area and reaching Liassic strata. Another field is the Jurassic petroleum system includes the Upper Liassic oil prone source rock (Posidonia Shale), the Middle Jurassic reservoir sandstones and the Middle Jurassic sealing shales (Magri et al. 2008). Here, the oil is stratigraphically trapped at the western flank of the salt diapir called Büsum made up of Zechstein and Rotliegend salt (Grassmann et al. 2005; Magri et al. 2008).
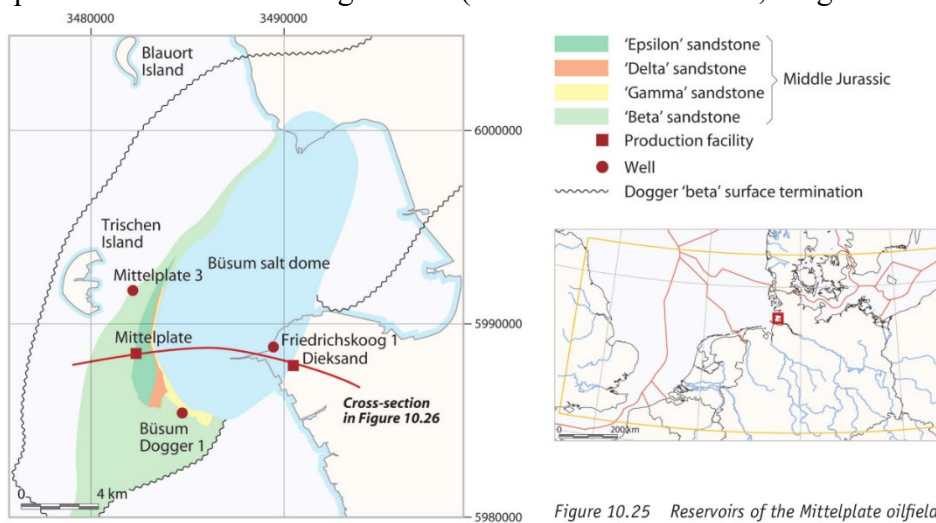
Figure 10.25   *Reservoirs of the Mittelplate oilfield.*

Fig. 3.14   Reservoirs of the Mittelplate oilfield (Petroleum Geological Atlas of the Southern Permian Basin Area, 2010).

About oil generation from the Liassic Posidonia Shale (Grassmann et al. 2005), this is generally immature to early mature or eroded in this area. The increased thermal maturity observed near the tops of the salt diapyrus may be a positive factor here (Rodon and Littke 2005; Magri et al. 2008). In eastern Germany, lateral migration over distances of tens of kilometres probably filled oil reservoirs in the Zechstein carbonates (Hindenberg 2000; Magri et al. 2008). In the Zechstein basin, as marls and fine-grained carbonates precipitated with higher organic carbon content and source rock potential, because the intraformational flow towards the most porous and permeable facies in the carbonates filled the rock salt-enclosed reservoirs (Magri et al. 2008).

3.2   Aims of the Cruise

(C. Hübscher)

In the course of the field exercise and in order to fulfill the pretension of combining education and research the student participants learn

- to install deck gear and lab instruments in accordance with safety instructions,
- to calculate a daily schedule, to communicate plans with the bridge,

- to prepare, maintain, deploy and retrieve a seismic source and a marine magnetometer/gradiometer,
- to process reflection seismic data with VISTA processing software (CMP-binning, bandpass filtering, gain, velocity determination, stack, poststack-time migration),
- to interpret collected data in terms of cruise specific scientific aims,
- to behave correctly in a closed, special working environment like a research vessel.

In order to demonstrate a research cruise, the following scientific objectives were selected:
- Identify shallow fault systems above a salt wall at northern Bay of Kiel and in Kadett Rinne.
- Identify and map glacial erosional unconformity around Rügen.
- Identify shallow gas and related imaging artefacts.
- Compare magnetic single sensor and gradiometer data.

3.3   Agenda of the Cruise

(C. Hübscher)

The cruise started and ended in Kiel (Fig. 3.15). The training of the students comprised several aspects. On deck, the preparation, deployment, recovery and maintenance of pneumatic seismic sources such as the GI-Gun was one centerpiece of the technical training. The students learned how to disassemble the device, clean, grease and reassemble it. In the lab, the student did regular shifts 24/7. They were 4 hours on duty with an interruption of 8 hours. During the watch free time, we continued with lectures on the instruments and data processing.
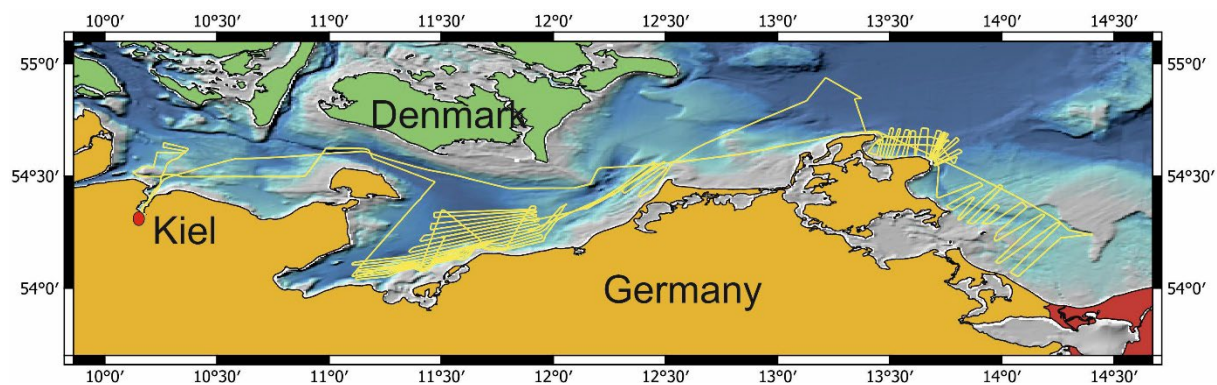
Fig. 3.15   Track chart of R/V ALKOR Cruise AL582.

Watchkeepers monitor the reflection seismic, magnetic and parametric echosounder systems. Besides the monitoring, we taught data processing with a strong focus on seismic data processing with Schlumberger's VISTA seismic processing software. The students set up the geometry (CMP-binning), determined bandpass filters depending on the seismic source, found an appropriate gain and performed a velocity determination. After the stack, a post-stack time migration was applied. Time migrated sections are available of almost all Profiles at the end of the cruise. Each late afternoon the entire group met at the science meeting and we discussed the Profiles of the last 24 hours. Underway findings were used to adapt the Profile layout. Measurements have been carried out in Bay of Kiel and Mecklenburg as well as east of Rügen.

4.   Narrative of the Cruise

(C. Hübscher)

On October 4 2022, the cruise participants met early in the morning in front of the GEOMAT-IKUM workshop hall to load the scientific equipment onto a truck. This was done around 09:30 and the group drove with three vehicles to Kiel to the GEOMAR pier on the eastern shore of the Kiel Fjord, where we were warmly welcomed by Captain Kaufmann and his crew of the research vessel RV ALKOR. Since the truck still had to clear its cargo with customs, there was enough time for the newcomers to familiarize themselves with the ship. A couple of drone flights allowed to take aerial photos of RV ALKOR and the RV LITTORINA in front of it. With strong support from the crew, the equipment was brought on deck with the ship's crane around noon. Afterwards the rigging of the labs and equipment on deck of the ship started, which could be finished in the early evening. In between, the newcomers on board received an intensive safety training by the chief mate.

RV ALKOR left the pier on October 5 at 08:00 and the transit to the first profiles started. North of Kiel lighthouse we first deployed the gradiometer magnetometer and started up the parametric sediment echosounder. The first profiles covered a crestal graben above a salt pillow in western Kiel Bight. After the magnetometer was retrieved in the early evening, further profiles passed the island of Fehmarn overnight to the northern Mecklenburg Bight, where seismic profiling began on October 6 in the morning with the deployment of the reflection seismic equipment. Due to rough seas, we used a very rugged 16-channel streamer only 100 m long and a 25/25 cubic inch seismic signal source for the measurements. The profiles ran near the 10-meter depth contour on the southern coast of Mecklenburg Bay. By the next day, the seas had calmed enough that 100 meters of streamers were exchanged for the so-called MicoEels with a total length of 200 meters. The generator and injector volumes were increased to 45/105 cubic inches. The profiles continued to run parallel to the south coast of the bay and over the "Trollergrund" salt pad. In the early morning hours of October 8, problems occurred in one streamer, so at 08:00 we brought both MicroEels on deck and deployed the 16-channel streamer again. By now all students had been instructed in data processing, so data was now being processed around the clock. Still the same day, we worked our way into the middle of Mecklenburg Bay with profiles parallel to the coast.

Three profiles surveyed during the night of October 10 across the coast-parallel profiles will later serve as the stratigraphic link between the profiles. A profile across the crest trench above the Trollergrund salt pillow we surveyed with reflection seismics three more times, but with different signal sources (Watergun, Sparker, Mini-GI) for training and comparison purposes. Later in the afternoon, we retrieved all the equipment towed in the water on deck and headed for our next work area, north du east of the island of Rügen. SES profiles surveyed during the night were used to search for shallow faults between Darss and Falster islands.

Seismic profiling started in the early morning of October 11 north of Kap Arkona (Rügen Island). The measurements during the next days around the Jasmund peninsula were used to map glacial erosion structures. After consultation with the ship's command, a helicopter flew in for an exercise in the early evening on 12.10. and dropped a rescuer on the working deck for a while as part of a drill, a small intermezzo of the tight work program. The last profiles were between the coast of

Usedom and the Oder fan. On October 14, the scientific measurement program ended in the early afternoon. When all instruments were on deck the transit back to Kiel started. Shortly after 08:00 am we reached the pier at the eastern shore of the Kiel Fjord, the expedition AL582 was finished.

5.   Preliminary Results

5.1   Installations

5.1.1   Lab Installations

(R. Zwetzich)

The main laboratory is located on the main deck and is the biggest room on FS ALKOR, besides the engine room and bridge. Inside, there is enough space for a customizable server rack, storage room, workspaces and computers for all given research purposes. During AL582, the laboratory (Fig. 5.1) contained the following workspaces including a specified computer:

1. Seismic Data Recorder
2. Seismic Source Trigger
3. Multibeam Monitoring
4. SES Data Monitoring
5. SES Data Conversion
6. one workspace for protocols only
7. two regular workspaces for students to run through processing seismic data
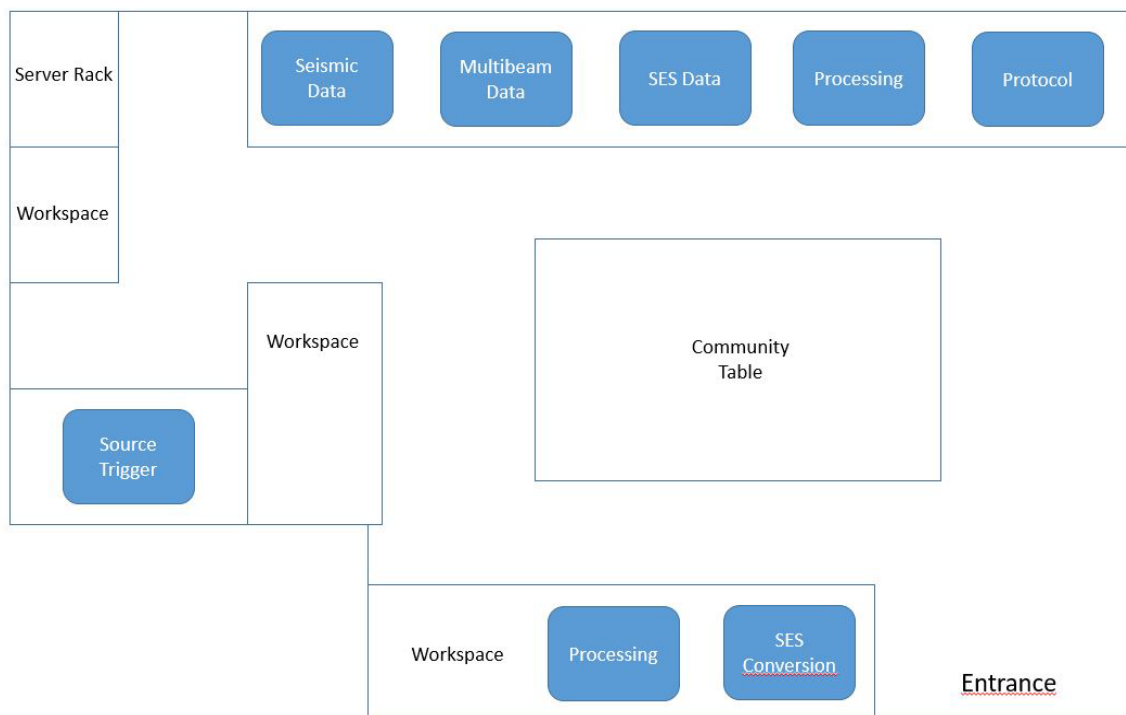
Fig. 5.1.   Sketch of lab arrangement (not to scale).

1. seismic data
The purpose of this workspace is collecting, and recording received seismic data and saving it in its hard drive for further processing purposes.

2. seismic source trigger

The displayed device is directly connected to the compressor container, triggering and maintaining the constant seismic shot interval (Fig. 5.2). The computer monitors the intensity, period and frequency of the seismic source. The PC is running on MS-DOS due to its undisputed reliability since there is no room for errors. Only when using the Sparker as a seismic source, the source trigger is not connected to the compressor. It is connected to the high-capacity generator instead.
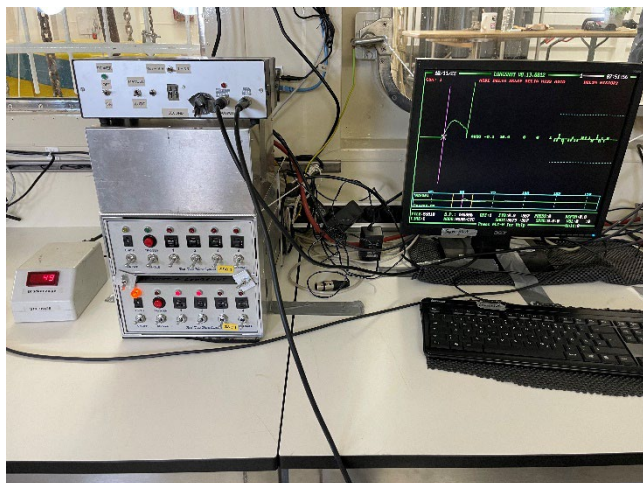
Fig. 5.2   Seismic Source Trigger Left: digital pressure gauge Center: trigger control console Right: trigger monitor

3. multibeam monitoring

This workspace is monitoring the Multibeam Echosounder MBES, an alternative to the SES Data when measuring water depth. It provides additional certainty when it comes to interpret SES data.

4. SES-data recording (Fig. 5.3)

Besides seismic data, SES data was one of the main aspects measured. It delivers a qualified proposition about the seafloors composition when dealing with seismic data at the same time. That is the reason why the main focus on each shift was the surveillance of the SES monitor. For storage purposes, the INNOMAR software only records data displayed in the corresponding window. The recording window was set to a length of 40m depth to track the multiple of the seafloor. Dependent of the current water depth, the seafloor was either mapped too high to be logged, or too low, leading to loss of information. To prevent any data loss, the offset had to be corrected at all times based on the actual water depth. The INNOMAR software records and saves data in .seg and .raw files, which had to be processed afterwards. During our cruise we made use of three frequencies: 5 kHz, 10 kHz and 15 kHz, however we focused the 5 kHz measurements.

5. SES data processing (Fig. 5.4)

The SES data processing is the next iteration of handling seismic data. In this process, the .raw files were converted into better interpretable SEG-Y files using special software.

6. protocol workspace

One workspace was dedicated to being used as a protocol (Fig. 5.3). Each time a new profile started, an important waypoint was reached, a profile ended or anything mentionable happened, an entry had to be made to ensure that the interpreter of the final seismic data has all necessary information available.

7. processing seismic data (Fig. 5.3)

There are two workspaces left in the laboratory, however the students spent most of their time on these PCs processing the recorded data and merging them with the respective position using VISTA. A detailed explanation what steps are needed to process seismic data is listed in chapter 5.4.

Fig. 5.3   different   workspaces   Left: SES   data   recorder   Center: seismic   processing   PC Right: protocol workspace

Fig. 5.4   different   workspaces   Left: SES   data   conversion   Center: seismic   processing   PC Right: private workspace

5.1.2   Deck Installations

(M. Wünsch)

Making the marine seismic measurements a possibility, installations on deck are needed. During AL582, the deck contained the following items, shown in Fig. 5.5.
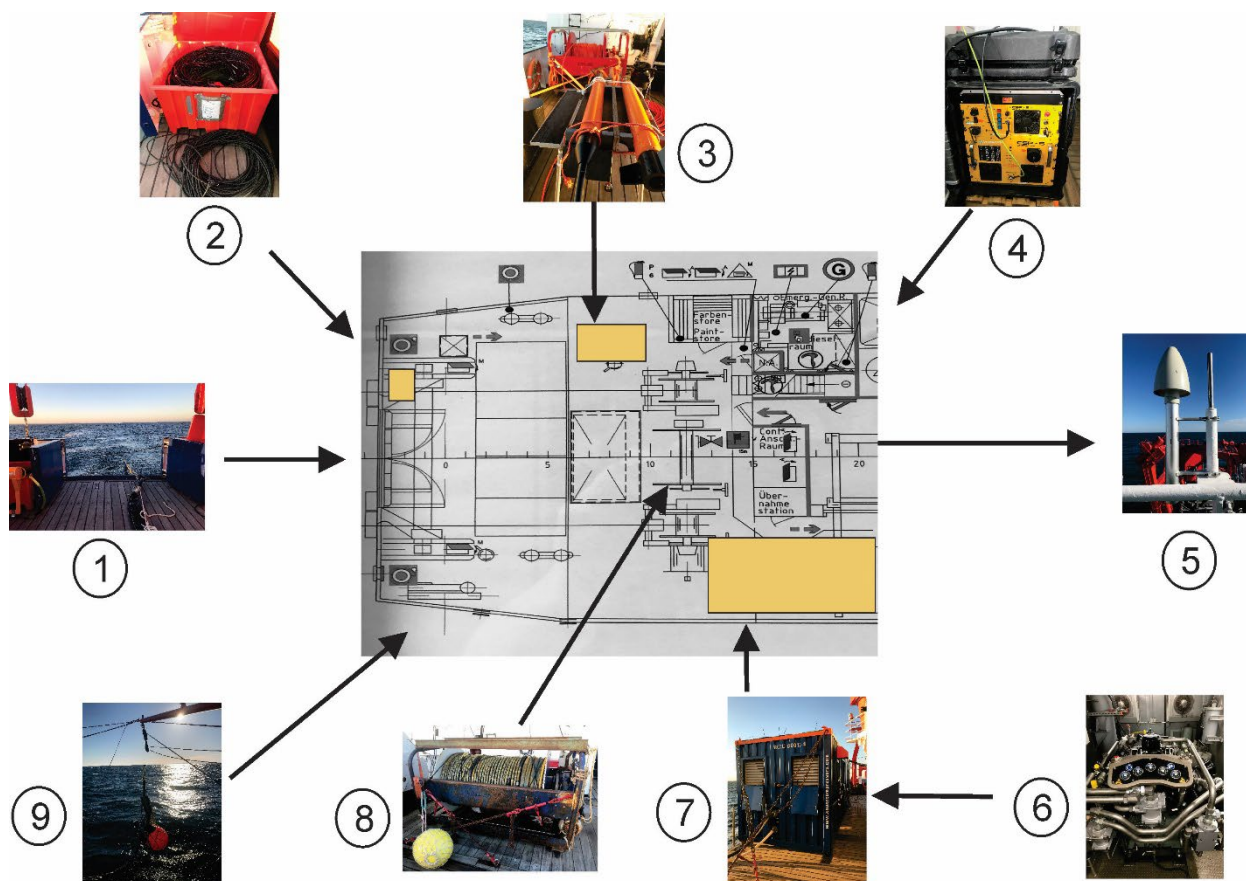
Fig. 5.5   Deck installations

1) Gate allowing a direct outlet for streamers.

2) Boxes Containing additional Streamers, for example the Micro-Eel Streamer.

3) Winch holding floating cable for two SeaSPY magnetometers (gradiometer), measuring magnetic gradient in one dimension by subtracting the difference between two independent magnetic sources.

4) CSPS-S Energy Unit with built-in high-capacity banks to generate short high voltage discharges for the Sparker.

5) GPS-Antenna providing accurate positional data.

6) HPAC (High Pressure Air Compressor) for seismic sources from Sauer.

7) Weather resistant ISO container, containing the compressor.

8) Analog Streamer on a winch.

9) Arm holding the seismic source and bringing it into position.

The geometry for the seismic acquisition is shown in Fig. 5.6.

Seismic Acquisition Geometry
onboard FS Alkor AL582 Expedition - 16 Channel Analog Streamer 04.10.22-15.10.22
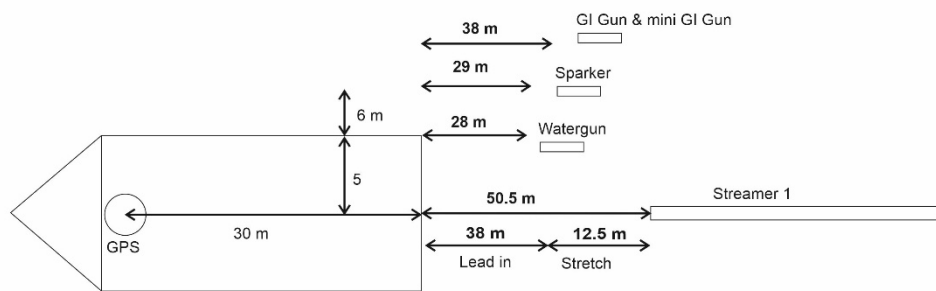
GI Gun & mini GI Gun
Offset along track: 68 m
Offset across track: 11 m

Sparker
Offset along track: 59 m
Offset across track: 0 m

Streamer
Offset CH 1 along track: 80.5 m
Offset across track: 0 m

Number of Channels: 16
Channel Spacing: 6.25 m

Watergun
Offset along track: 58 m
Offset across track: 11 m

Fig. 5.6   Seismic Acquisition Geometry onboard FS ALKOR AL582

5.2   Reflection Seismic Equipment

5.2.1   Marine Seismic Sources

(G. Hampel, R. Zwetzich)

5.2.1.1   Basics

An essential part of marine seismic measurements is the source, generating an acoustic signal, which is later captured and recorded by streamer cables. In most cases the seismic source emits an impulse, reflecting from seafloor and underlying layers and generating the signal. An important aspect when choosing the right source is finding the correct compromise between limiting factors, i.e water depth, penetration depth, resolution and frequency spectrum. Each of the following sources has its own advantages and disadvantages, which are listed below.

The ideal signal of the seismic source is a single peak or delta pulse when looking into the amplitude spectrum. If we have a look into the frequency spectrum, the bandwidth would be infinite. There are several reasons why this ideal signal does not exist: The formation of two major signatures: The Ghost signal and Bubble signal. Due to the hydrostatic pressure equilibrium, the air bubble resulting from the detonation transcends to an oscillating process, producing unwanted noises, resulting the Bubble Signal. The Ghost signal is once more an undesired effect, which is caused by the reflection of the primary signal at the sea surface and the following phase reversal due to the reflection coefficient between air and water. This causes a time shifted arrival of the signal at the seafloor, the Ghost signal. This also causes the so-called "Ghost notch" in the frequency spectrum, which can be calculated

$$\text{frequency}_{\text{ghost}} = \text{velocity}_{\text{water}} / 2* \text{ towing depth}$$

Dealing with the ghost signal is always finding the right compromise between water depth and maximum available resolution. Lowering the frequency will improve the penetration depth but will worsen the resolution. The best option in this case is to choose a towing depth where the notch is located at a higher frequency than the fundamental frequency.

5.2.1.2   Airgun

The Airgun consists of a heavy metal container, generating an air bubble after releasing a by rapidly releasing highly pressurized air. To reduce the earlier mentioned Bubble signal, the so-called G.I. Gun (Generator – Injector Gun) injects a time shifted, second air bubble into the first generated bubble to withstand the outer hydrostatic pressure and stopping the oscillating process, gaining clearer data acquisitions. The G.I Gun can be used into different operating modes:
Harmonic Mode: In this case, the volume of the two air chambers is evenly distributed. The Generator and the Injector each contain 25 cubic inches respectively with a pressure of 150 bar on each shuttle valve. This mode induces a signal with an amplitude peak of 100 Hz.
True GI Mode: The Injector releases a significant higher volume than the first generated bubble to minimize undesired frequency noise due to the already mentioned oscillating process. The Generator compresses 45 cubic inches to 150 bar whilst the Injector, the second bubble, generates a pressurized volume of 105 cubic inches. This mode induces a signal with an amplitude peak of 150 Hz.

5.2.1.3   Mini G.I. Gun

The Mini G.I Gun (Fig. 5.7) is a smaller version of the earlier mentioned G.I. Gun. Each shuttle valve contains not more than 30 cubic inches, also compressed up to 150 bar. Whilst the generator contains a volume of 15 cubic inches in our configuration, the Injector doubles those volumes to 30 cubic inches and fulfils the True G.I mode of the regular airgun-The produced signal has a higher frequency compared to the G.I Gun up to 200-300 Hz and a more broad banded frequency spectrum. An advantage of the Mini G.I Gun is its good performance in shallow waters, however, due to the higher frequency compared to the regular airgun, the penetration depth is poorer.

Fig. 5.7   Mini G.I Gun (left) with adjustable buoy for depth control.

5.2.1.4   Watergun

In contrast to the Airgun, the Waterguns (Fig. 5.8) working principle does not rely on compressing air. Instead, it rapidly compresses water in a cylindrical chamber, which resolves to an instant vaporization, causing a thermodynamic implosion subsequently. In our case, the Watergun is used with an operating pressure of 190 bar and a shot rate of four seconds. The result is a low-amplitude and highly broad banded frequency between 100 Hz and 800 Hz. The Watergun results as a low-cost solution and an alternative for the Mini G.I Gun but lacks also in penetration depth. The resolution, however, is remarkably good.

Fig. 5.8   Watergun (below) with adjustable buoy for depth control.

5.2.1.5 Sparker

Unlike all other mentioned sources, the Sparker (Fig. 5.9) does not use any kind of compression, neither air nor water. Instead, the Sparker has six short-circuited electrodes with an operating input voltage of 4 kV. Beforehand, the voltage gets amplified and transformed by high capacity banks, supplied by a high voltage current cable. These short discharges a highly energetic electric arc, which, similar to the Watergun above, leads to an instant vaporization and an immediate implosion causing an acoustic blast. The provided energy amounts 3000 Joules at a shot rate of four seconds. The result is a very low frequent and high amplitude spike around 100 Hz with a not mentionable bandwidth.

Fig. 5.9   Sparker (left) with adjustable buoys for depth control. CSP-S Energy Unit (right) with built-in high-capacity banks to generate short high voltage discharges.

5.2.2   Seismic sources: a comparison

Whilst the True-Gi Mode operates with a volume ratio of 45 to 105 cu.inch, the much smaller configured harmonic mode operates with a ratio of 25 to 25 cu.inch. As you can see in Fig. 5.10 and 5.11, the amplitude of the True Gi Mode is higher to than its contender (True-GI: 180 vs Harmonic: 150), due to its much higher generator volume. In addition to that, the True GI Mode shows a bigger bandwidth than in Harmonic mode (True-GI: 180 Hz vs Harmonic: 110 Hz). This is lead back to the properties of the True GI Gun with its higher Injector volume as well and because the main function of the True Gi mode is supressing the bubble signal. As we know, a bigger bandwidth results in a better compromise between resolution and penetration depth.
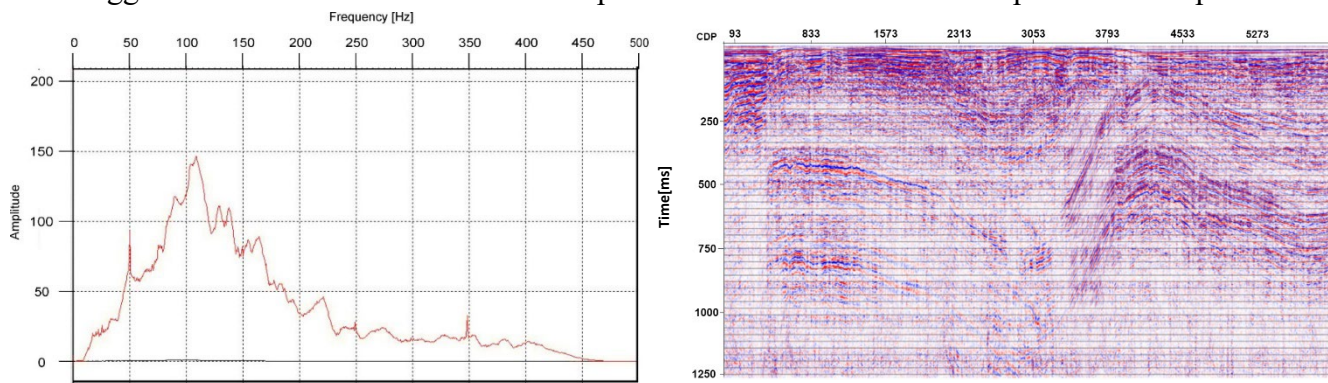
Fig. 5.10   GI Gun – Harmonic Mode (25 to 25) left: Amplitude spectrum, right: seismic section (Profile 3)
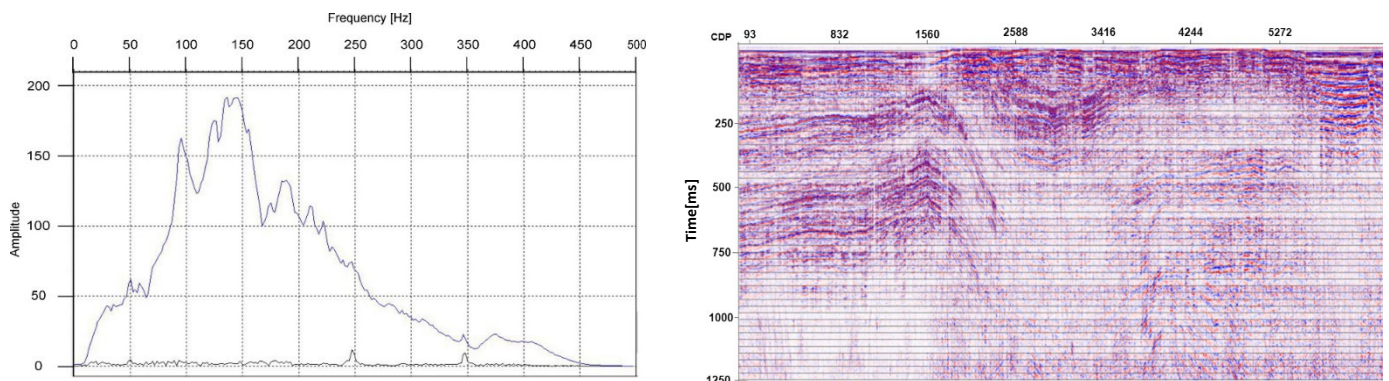
Fig. 5.11   GI Gun – True GI Mode (45 to 105) left: amplitude spectrum, right: seismic section (Profile 4)

Comparison of Sparker, Watergun and Mini-GI:

All of these three seismic sources operate with different procedures as mentioned in chapter above According to that, all of them have different energy signatures. The sparker (Fig. 5.14), with its high voltage capacitor banks, results in a much higher amplitude of over 1000, than its competitors but with a much smaller bandwidth around 30-50 Hz and an obvious visible bubble signal.

In comparison to that, the Watergun (Fig. 5.12) has less powerful amplitude due to its working principle. However, this device provides the highest bandwidth of all compared seismic sources, including the original GI Gun of nearly 780 Hz which has its own advantages in interpretation seismic data. The Mini-GI however, is misrepresented. Both, the amplitude and the frequency spectrum are higher in relation than its direct contester, the GI Gun, either in True-GI or in Harmonic Mode, although the Mini GI provides a much smaller volume. It does not seem logical to

us, why the energy signature of the Mini GI (Fig. 5.13) has a much better performance. One reason for this may be the difference in towing and water depth.
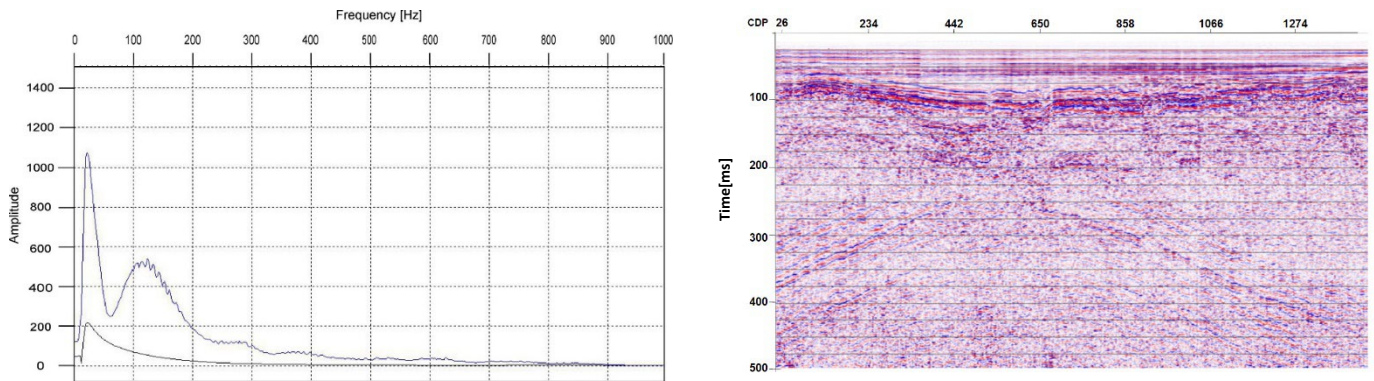
Fig. 5.12   Left: Amplitude spectrum of the Watergun, right: Seismic section (Profile 22)
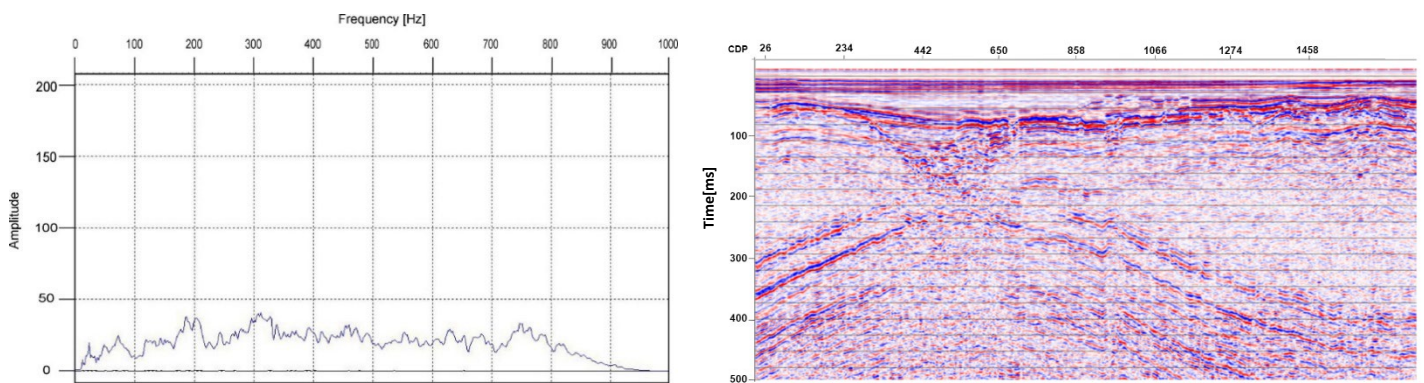
Fig. 5.13   Left: Amplitude spectrum of the Mini G, right: Seismic section (Profile 24)
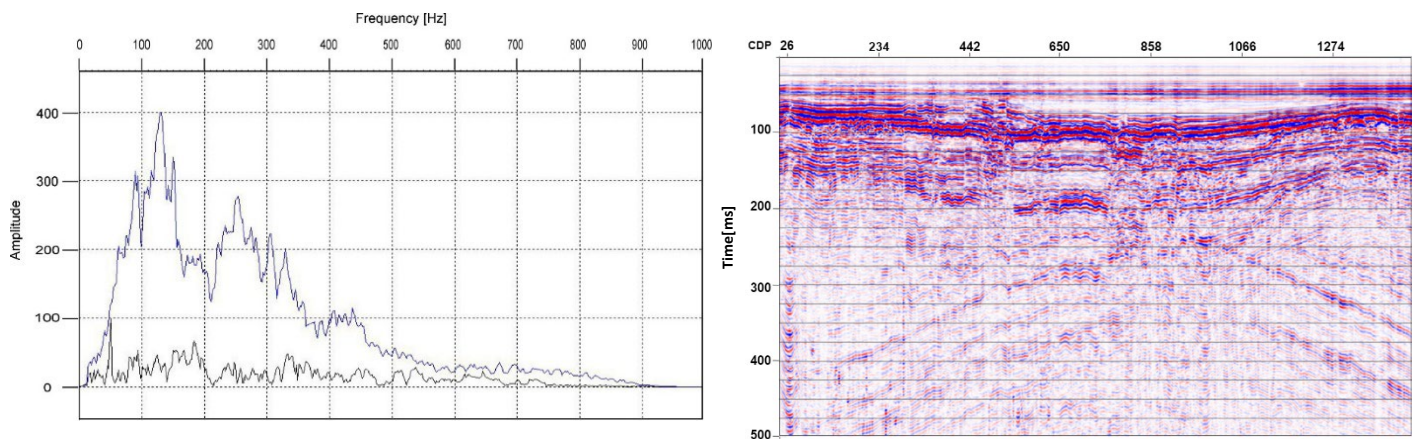
Fig. 5.14   Right: Amplitude spectrum of the Sparker, left: Seismic section (Profile 23)

5.3   **Streamer**

(G. Hampel, R. Zwetzich)

The purpose of the marine seismic streamer is the capturing and converting of acoustic signals to an electrical signal. Therefore, there are two types of streamer cables in use. Both streamers are towed behind the vessel, while the cable length can be modified to the preferred usage. During our cruise, we used both versions of the streamers, to point out the advantages and disadvantages of each kind.

5.3.1   16 Channel Analog Streamer

The first one, the analog streamer, shown in Fig. 5.15, consists of 16 hydrophone groups or so-called "channels", which again includes eight single hydrophones without any active pre-amplifiers. The analog streamer is mounted on a stationary electric winch, which is connected to the laboratory for further data recording and processing. To prevent any towing damages to the active streamer section, the cable starts with a lead-in cable, which withstands the upcoming drag force. Due to undesired noise caused by ship movements, engines and the tail buoy, the lead-in cable and the active streamer section is connected with an elastic stretch section. Usually, there are additional birds in use to control the towing depth of the streamer but due to the shallow water depths and the relatively short streamer cable, the reduced buoyancy of the freshwater, they were not necessary and therefore not attached to the cable. To prevent the streamer from uplift to the surface and to ensure the transmission to the piezo-electric ceramic sensors, the plastic membrane is rather filled with ISOPAR M, a fluid with lower density than water.

During our cruise, we used the following streamer configuration:

Analog Streamer

Channel Quantity	16
Hydrophones per Channel	8
Channel spacing [m]	6.25
Lead-in [m]	38
Stretch section [m]	12.5
Active length [m]	100
Total [m]	150.5

Table 5.1   Streamer configuration

Fig. 5.15   16 Channel Analog Streamer.

5.3.2   24 Channel Micro Eel Streamer

The Micro-Eel (Fig. 5.16) digital streamer includes 24 channels, with 12 hydrophones each. The Micro-Eel cable also amplifies the captured data and transforms into a digital signal. In contrast to the analog streamer, the Micro Eel cable is not mounted on a stationary winch. Instead, the cable must be released into the water by hand. To prevent any towing damages to the active streamer section, the cable starts with a lead-in cable (Fig. 5.16), which withstands the upcoming drag force.

Since the hydrophones are completely molded into plastic, the streamer is not dependent of additional control birds or additional buoyancy fluids. Although, there were lead lines for additional weight to prevent the streamer from breaking the surface. The features of the outer plastic layer is similar to the purpose of the stretch section of the analog streamer.

Fig. 5.16 4 Channel Micro-Eel Streamer.

During our cruise, we used the following streamer configuration:

Micro-Eel Streamer	1	2
Channel Quantity	24	24
Hydrophones per Channel	12	12
Channel spacing [m]	4	4
Lead-in [m]	75	175
Active length [m]	100	100
Total [m]	175	275

Table 5.2 Micro-Eel streamer configuration.

5.3.3   Conclusion

Since the analog 16 Channel streamer has a stretch section, it is more suitable for rough weather conditions, but due to the bigger channel spacing it lacks in coverage and therefore, has a poorer resolution. As shown in the example seismic section in Fig. 5.17.
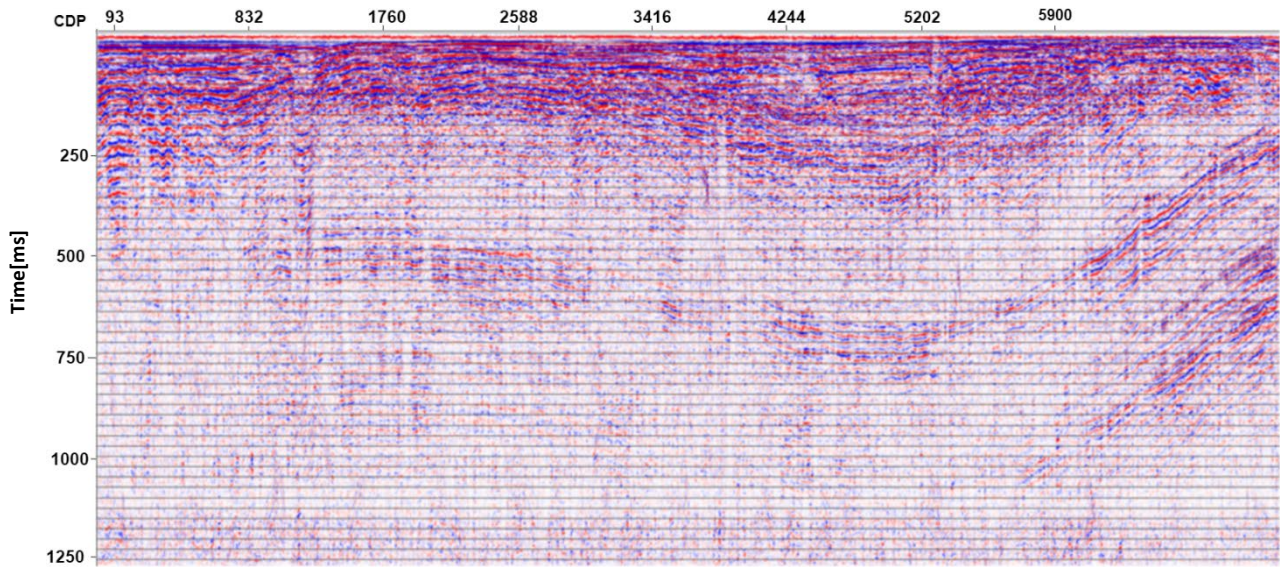
Fig 5.17   Seismic section (Profile 6) recorded with Analogstreamer

The resolution of the Micro-Eel is much better because of its lower channel spacing of 4m, instead of 6.25m regarding the analog streamer, but the data suffers from noise caused by waves, engines and ship movements. This is displayed in Fig. 5.18.
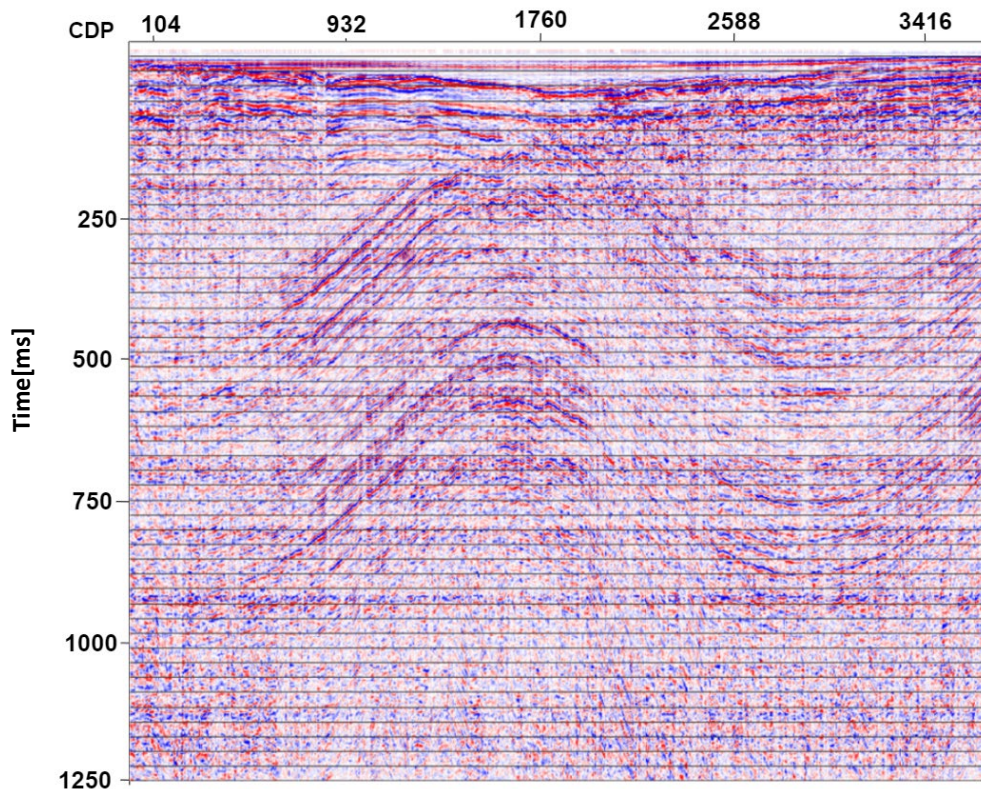
Fig 5.18   Seismic section (Profile 10) recorded with MircoEel

5.4   Seismic Data Recording

(G. Hampel, R. Oelkers)

Profile No.	Seismic Source	SeismicRe-ceiver	Shot In-terval	GI Delay	Sam-pling Rate	Pressure /Energy
MCS001	GI Gun (25/25)	16-Channel	5 sec	24 ms	0.5 ms	150bar
MCS002						
MCS003						
MCS004	GI Gun (45/105)					
MCS005		Micro Eel				
MCS006						
MCS007						
MCS008		16-Channel				
MCS009						
MCS010						
MCS011						
MCS012						
MCS013						
MCS014						
MCS015						
MCS016						
MCS017						
MCS018						
MCS019						
MCS020						
MCS021						
MCS022	Water Gun		4 sec			190 bar
MCS023	Sparker					3 kJ
MCS024-MCS076	Mini GI		4 sec			150 bar

Table 5.3   Recording parameters for different seismic methods.

For triggering the GI Gun and the recording, a trigger PC was used. The shot interval, the aiming point of the shot itself as well as the delay between Generator and injector (GI-Delay) could man-ually be adjusted. Mounted on the GI Gun is a hydrophone that connects to the trigger pc to review the generated Signal to set the optimal time delay between Generator and injector to suppress the

Bubble signal. The trigger signal then was amplified. To ensure the correct and constant air pressure, an additional display monitored the present pressure value. The analog signal from the 16-channel streamer as well as the micro-Eel was digitalized with an analog to digital geode converter. The digitalized signal was recorded on a different (recording) PC that also showed the current shot gather and channel stack for quality control. A GPS arrived timestamp ensured the precise recording time. The triggering and recording parameters for the different seismic methods are shown at table 5.3:

5.5　　　Data Processing

(G. Hampel, R. Oelkers)

The seismic Data was processed by using Vista by Schlumberger. In the following, each processing step (flow) is briefly described. An Overview of this process can be seen in Fig. 5.19.

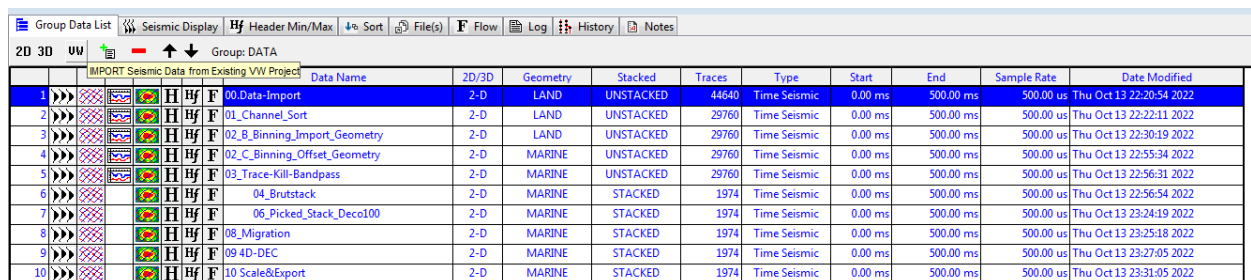|	Data Name	2D/3D	Geometry	Stacked	Traces	Type	Start	End	Sample Rate	Date Modified
1	00.Data-Import	2-D	LAND	UNSTACKED	44640	Time Seismic	0.00 ms	500.00 ms	500.00 us	Thu Oct 13 22:20:54 2022
2	01_Channel_Sort	2-D	LAND	UNSTACKED	29760	Time Seismic	0.00 ms	500.00 ms	500.00 us	Thu Oct 13 22:22:11 2022
3	02_B_Binning_Import_Geometry	2-D	LAND	UNSTACKED	29760	Time Seismic	0.00 ms	500.00 ms	500.00 us	Thu Oct 13 22:30:19 2022
4	02_C_Binning_Offset_Geometry	2-D	MARINE	UNSTACKED	29760	Time Seismic	0.00 ms	500.00 ms	500.00 us	Thu Oct 13 22:55:34 2022
5	03_Trace-Kill-Bandpass	2-D	MARINE	UNSTACKED	29760	Time Seismic	0.00 ms	500.00 ms	500.00 us	Thu Oct 13 22:56:31 2022
6	04_Brutstack	2-D	MARINE	STACKED	1974	Time Seismic	0.00 ms	500.00 ms	500.00 us	Thu Oct 13 22:56:54 2022
7	06_Picked_Stack_Deco100	2-D	MARINE	STACKED	1974	Time Seismic	0.00 ms	500.00 ms	500.00 us	Thu Oct 13 23:24:19 2022
8	08_Migration	2-D	MARINE	STACKED	1974	Time Seismic	0.00 ms	500.00 ms	500.00 us	Thu Oct 13 23:25:18 2022
9	09 4D-DEC	2-D	MARINE	STACKED	1974	Time Seismic	0.00 ms	500.00 ms	500.00 us	Thu Oct 13 23:27:05 2022
10	10 Scale&Export	2-D	MARINE	STACKED	1974	Time Seismic	0.00 ms	500.00 ms	500.00 us	Thu Oct 13 23:31:05 2022

Fig. 5.19　　　Screenshot from all flows of an already processed seismic profile

<u>00_Data_Import</u>
In the first flow the raw shot data from the analog streamers are imported into Vista, then the shot point number is assigned into the field record number in the header.
<u>01_Channel_Sort</u>
Since the first 1-9 channels are broken, they are deleted.
<u>02_A_Binning_Export</u>
Creates an ASCII file with a timeline from all the seismic records, to merge it in the next processing step with the ship's coordinates.
<u>02_B_Binning_Import_Geometry</u>
The seismic records are merged with the ships position records, taking in account the distance between GPS antenna and the seismic source as well as the streamer. The Output od this step is shown in Fig. 5.20.
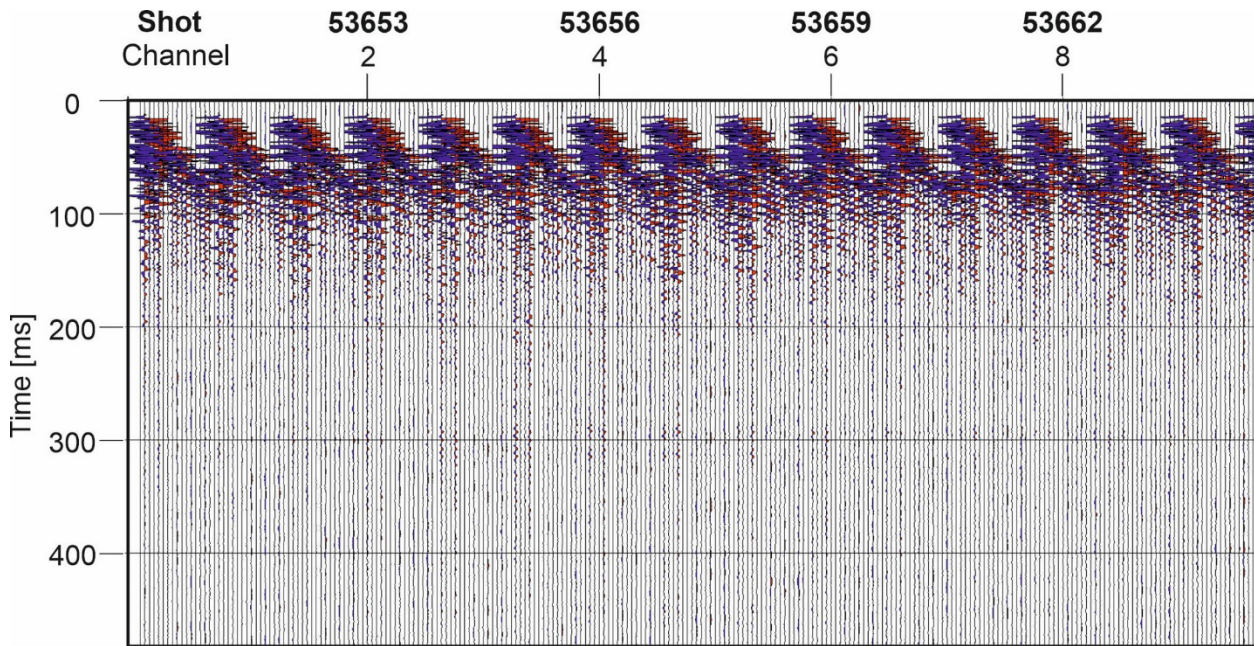
Fig. 5.20   Example for the 02_B_Binning_Import_Geometry output

02_C_Offset_Geometry

Because the seismic source and hydrophones are offset (as seen in Figure 5.6 the seismic source is not in line with the seismic receiver), the correct distance between each Hydrophone and the seismic source had to be estimated. Therefore, the time of the direct wave signal was approximated manually by considering the mean of 6-8 Shot-Gathers. By assuming a constant water velocity of 1500 m/s the distance and therefor the offset could be corrected. An example for that process can be seen in Figure 5.21.

MCS-P068_P07 Channel		53650	53893	54165	54378	54720	54957		Mittelwert in s	Distanz in m
Shot Number:										
	1		10.51	10.39	10.21	10.39	11.12		0.010524	14.8
	2	13.6	13.54	13.54	13.54	13.6	13.35		0.013528333	20.2925
	3	17.22	17.22	17.04	17.16	17.1	17.46		0.0172	25.8
	4	20.55	20.91	20.61	21.03	20.79	21.33		0.02087	31.305
	5	24.35	24.53	24.35	24.78	24.53	25.14		0.024613333	36.92
	6	28.16	28.28	28.52	28.58	28.64	28.64		0.02847	42.705
	7		Keine		Zahlen		Eintragen			48.93125
	8	36.38	36.62	36.8	36.5	36.86	37.47		0.036771667	55.1575
	9	41.03	41.82	41.52	41.88	41.39	42.78		0.041736667	62.605
	10	44.72	45.08	45.08	44.96	45.69	45.38		0.045151667	67.7275
									11	73.9775
									12	80.2275
									13	86.4775
									14	92.7275
									15	98.9775
									16	105.2275

Zahlen eintragen von der Shot Number

und den dazugehörigen Werten

Das ist die direkte Wave

Fig. 5.21   Example for picking the direct wave signal and calculating the approx. Distance between seismic source and receiver.

Binning

Is not a flow itself but a revision of the data quality and rearrangement of the Shot-Gathers into Common-Midpoint-Gather (CMP) by creating bins for every CMP.

03_Trace_Kill_Bandpass

The amplitudes are scaled equally; all temporally silent and overlayed (only noise) channels are deleted from the CMP-Gather and a band-pass filter is used to filter all unwanted frequencies (10Hz, 20Hz, 600Hz, 1200Hz).

04_Brutstack

The single CMP-Gathers are stacked by using a depth constant velocity of 1500 m/s and correcting the signal loss caused by the geometric dispersion loss. An example result for this step ist shown in Fig. 5.22.
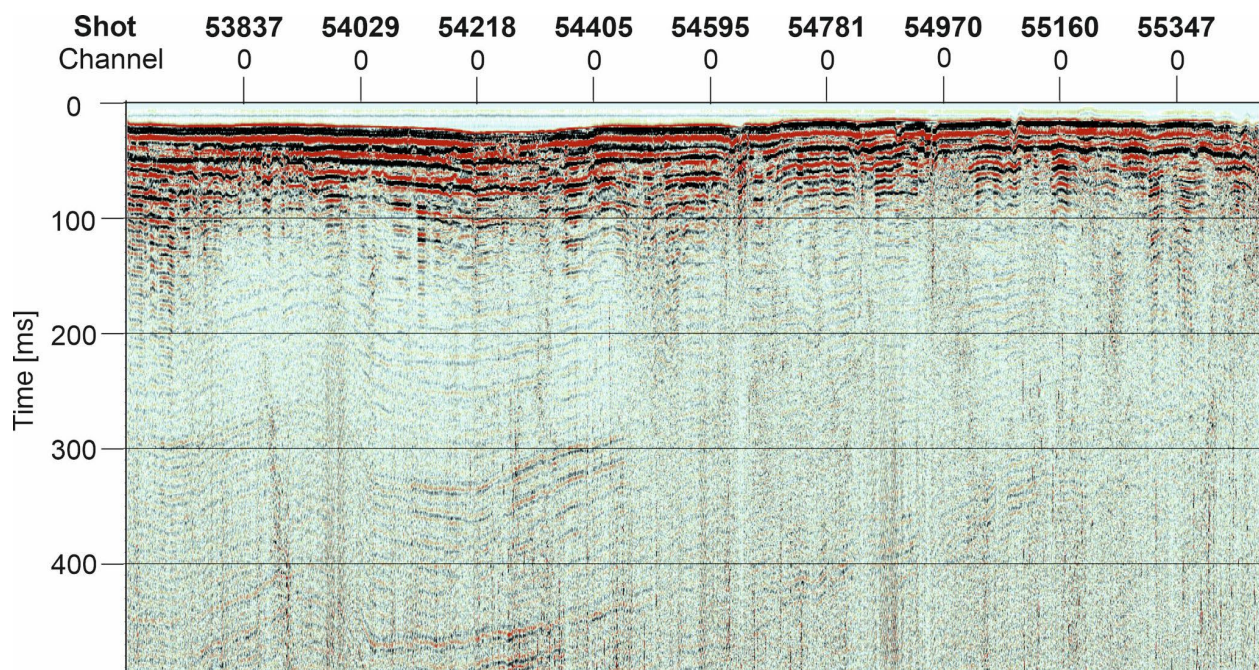
Fig. 5.22   Example for an Brutstack

05 Velocity Picking

The Root-Mean-Square-Velocity (RMS) for each detectible Strata is picked manually. An example for this can be seen in Fig. 5.23.

06_Picked_Stack_Deco100

The Brutstack flow is now repeated once again, but this time with the manually picked RMS-Velocities. Furthermore, the updated Brutstack is deconvoluted to reduce multiples.

08_Migration

A Migration is done to prevent diffractions and to increase the resolution.

09_4D_Dec

This flow consists of many steps to remove white noise from the seismic data, according to Patrick Butler.

10_Scale&Export

For better identifiability the lateral continuity is increased and a final scaling of the RMS-Velocity is done. The output is exported as an SEG-Y file, shown in Fig. 5.24.
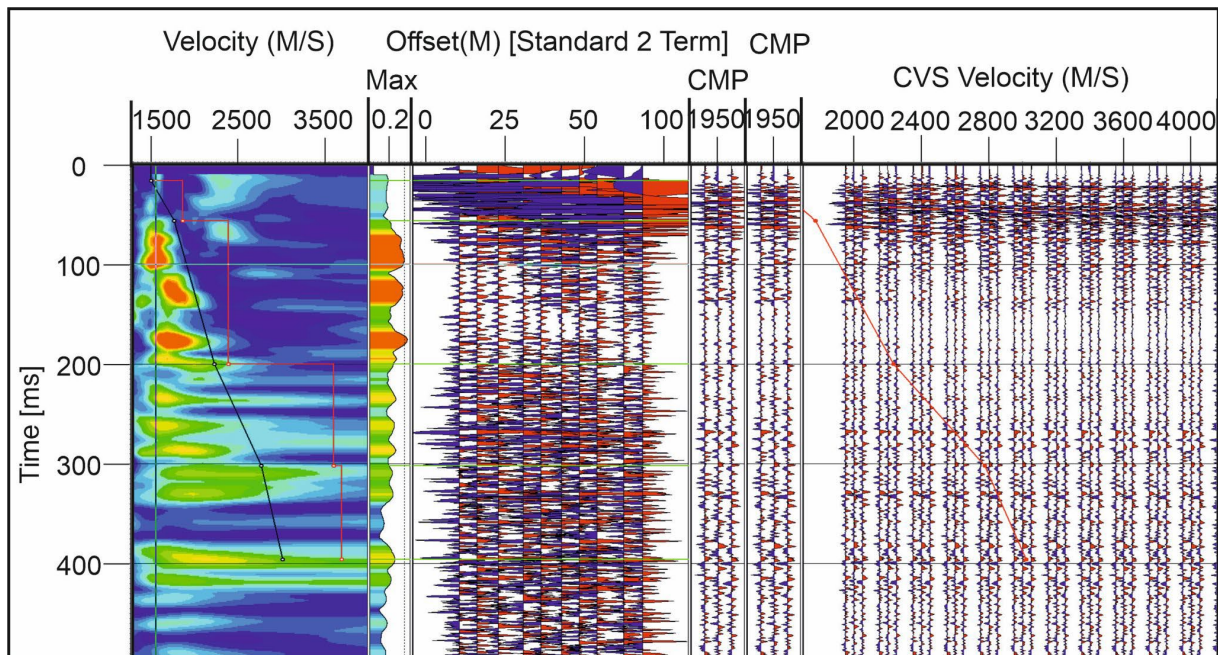
Fig. 5.23   Example for picking the RMS-Velocity
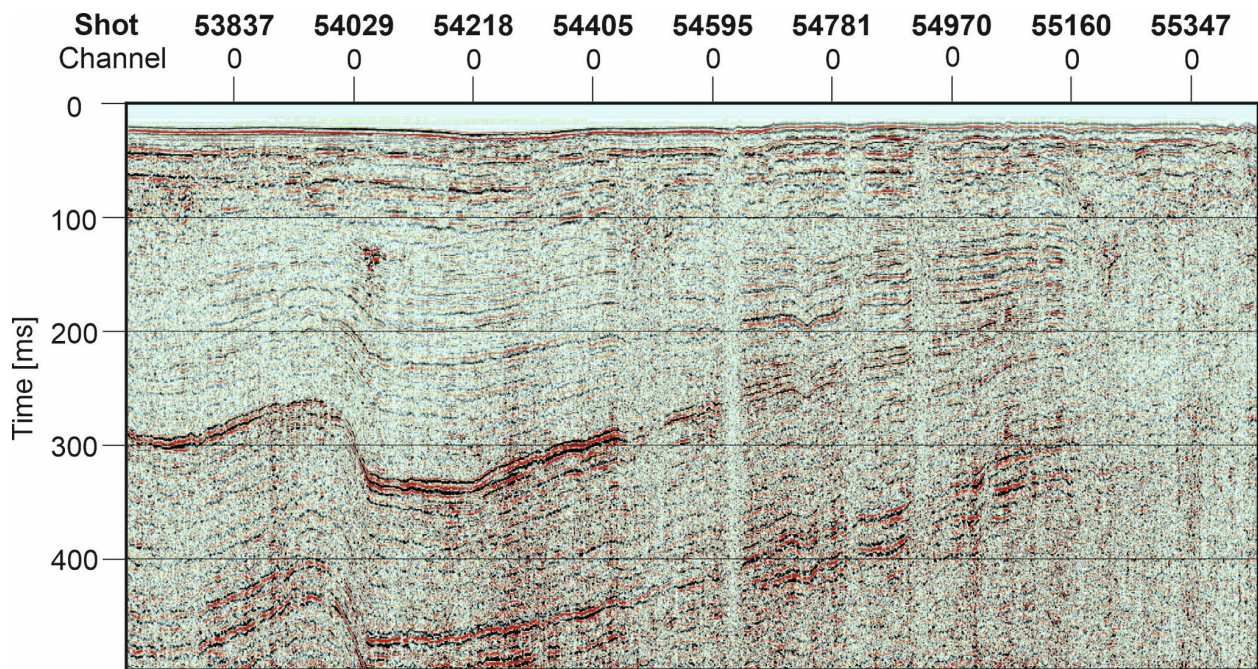
Fig. 5.24   Example of a final processed seismic profile

5.6   **Hydroacoustics**

(A. Wintermeyer)

5.6.1   **Parametric Sediment Subbottom Profiler**

The SES is a parametric sub bottom profiler, a sediment echo sounder used to examine the upper layers of the seafloor, particularly the sediment layers. A parametric echo sounder utilizes sound waves to penetrate the seafloor and records the two way time of the different reflections.

The system consists of the source for the sound waves, a so-called transducer, a mechanism to compensate the ships movement, and the technology on the ship like the computer with the recording software. The transducer is installed underneath the hull of the ship and consists of piezoelectric elements that functions both as source and receiver. The piezoelectric elements are phase controlled which allows for directional control over the sound cone. That in combination with mechanisms to detect the ships movement allows heave and roll correction to minimize distortions in the data. The technology on the ship includes a computer for the data collection with the recording software, displayed in Fig. 5.25.

For better penetration of the seafloor lower frequencies are preferable. To directly generate a signal of the frequency needed a very large Transducer would be needed. The SES system is a parametric one, which means instead of directly generating a sound pulse of the preferred frequency the parametric effect is used. The parametric effect is a phenomenon that occurs in sound propagation at high pressure. It causes two signals to interact with each other and create a third and fourth signal whose frequencies consists of the difference and the sum of the original two frequencies ($f3 = f1 - f2$, $f4 = f1 + f2$). This allows for transducers of a much smaller size.

The SES system uses two signals with frequencies around 100 kHz to create the signals used for the exploration with frequencies of 5, 10 and 15 kHz.

To record the collected data the SESWIN software was used. During the cruise the frequencies 5 10 and 15 kHz where recorded. The recording window was set to a length of 40 m, but the starting

point had to be adjusted manually (Fig. 5.25), depending on the water depth and the area that was of interest. Only the data that was visible in the recording window got saved.

Additional information recorded and visible in the recording software were noted as: SIS1 (longitude degree decimal minute), SIS2 (latitude degree decimal minute), SIS3 (UTC time), SIS4 (longitude degree decimal minute), SIS5 (UTM X), SIS6 (UTM Y) and SIS7 (MRU, motion sensor).
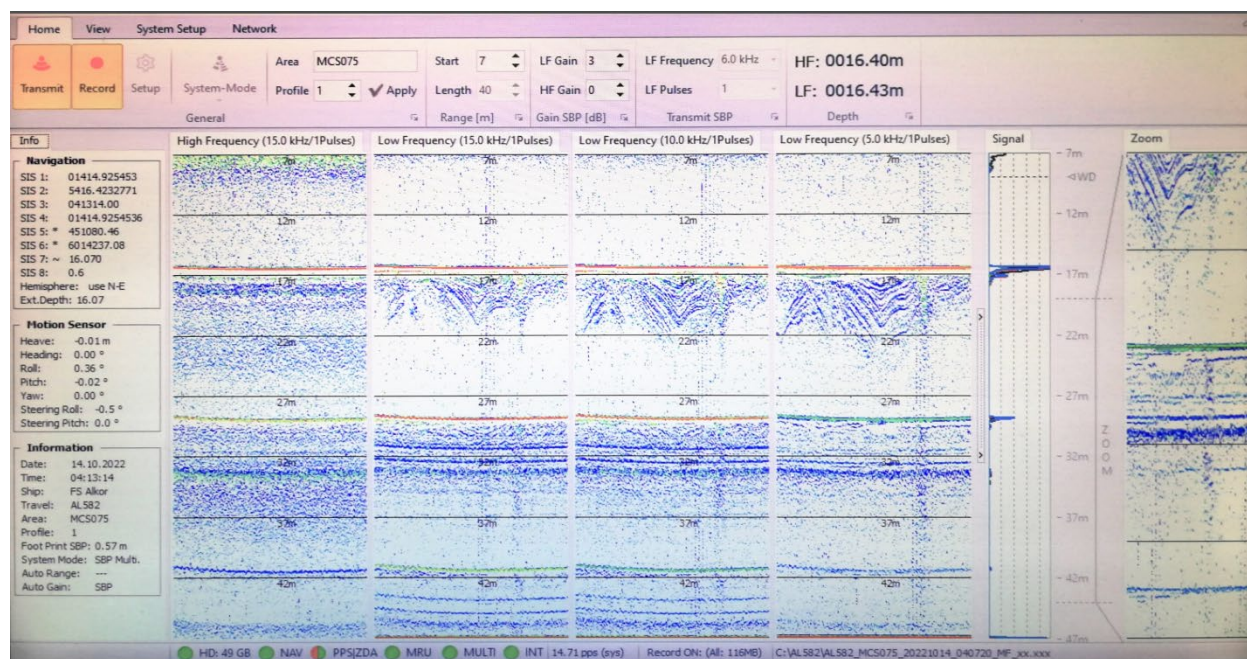
Fig. 5.25   Picture of the SESWIN recording software

The SES data recorded was save in the following naming format:

AL582_MCSXXX_YYYYMMDD_HHMMSS

MCSXXX   the profile during which the data was recorded.
YYYYMMDD   (year/month/day) the date in UTC time it was recorded
HHMMSS   (hour/minute/second) the time in UTC time.

During the AL582 cruise the SES data was recorded for information on glacial tectonics. The data was collected for information on either the reactivation of old folds due to glacial tectonic or the general structure of the glacial erosion and tectonic structures, particular in the area around Rügen (Fig. 5.26), in an attempt to later reconstruct the processes that caused them.
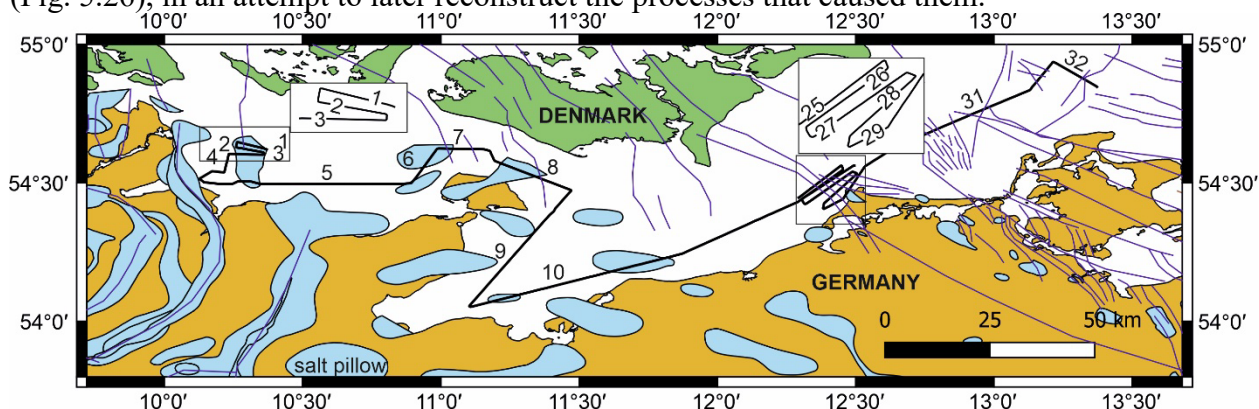
Fig. 5.26   Light blue areas indicate salt pillows or salt walls. Dark blue lines are representing tectonic folds.

5.6.2   Swath Sounder

The SEABEAM 3100 is a multibeam echosounder operated with the HydroStar software. The multibeam echosounder is a system to map out large areas of the seafloor by recording the reflection time and using multiple sound beams at once. The system is mounted underneath the hull and can be run simultaneously to the other systems, giving information on the seafloor surface that can be linked with the other recorded profiles. During the AL582 cruise the SEABEAM was use with a beam angel of 120 degrees.

5.7   Magnetics

         (L. Ischebeck)

Two magnetic measurements were executed during the cruise. This was mainly for the purpose of testing instruments and setup.

The SeaSPY magnetometer, by Marine Magnetic's, was used in a longitudinal setup. The instrument can be seen in Fig. 5.27. shortly before it was deployed into the water. It measures the magnetic gradient in one dimension. This is done by subtracting the measured values of two independent Overhauser magnetometers, that were towed behind each other with a distance of 100m and a total distance from the ship of 500m. With a range of 18,000nT to 120,000nT and a sampling rate between 4 Hz and 0.1 Hz, we can measure with an absolute accuracy of 0,1 nT (Hrvoic, 2007). When used as a gradiometer no corrections are necessary. The Lab installation setup used for recording and processing can be seen in Fig. 5.28.

Fig. 5.27   SeaSPY magnetometers, with 400m towing length (on the winch in the background) and additional 100m in between the sensors (on the deck)
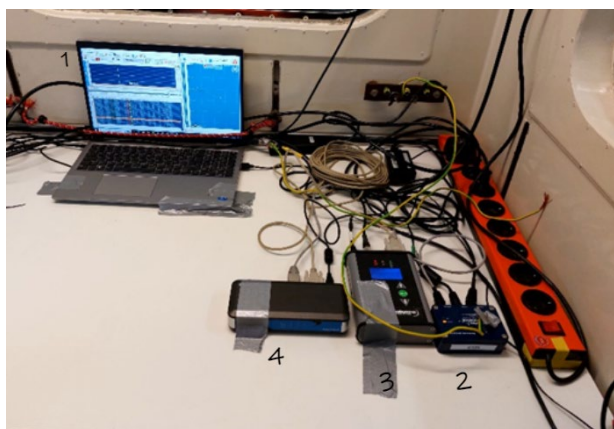
Fig. 6.28 Lab installation of the magnetometer.

5.8 First Results

Since the location of the profiles were specifically chosen to complete the crustal structural data of the Bay of Mecklenburg and Bay of Kiel, it was important to verify that the new recorded data matches up with the existing ones for quality and resolution control.

Significant and characteristic structures that were observed during the processing of the SES and seismic data were discussed and compared to already existing data.

Using those already existing data it was possible to locate most of the characteristic structures in the new data and gave the needed information for choosing the right combination of seismic source and receiver for optimal data quality.

If the new recorded data is sufficient for further studies of the Baltic Sector of the North German Basin remains to be seen.

6   Ship's Meteorological Station

(M. Wünsch)

Date (MM.DD.YYYY)	Day	hour	wind force 10m	wind direction in 10m	sig. wave height	weather
		UTC	Beaufort	Windrose	m	
10.05.2022	Wed	6	4-5	SW	1	
10.05.2022	Wed	12	4-5	SW	1	
10.05.2022	Wed	18	5	SW	1.5	
10.06.2022	Thu	0	5-6	SW-S	1.5	
10.06.2022	Thu	6	6	SW-S	1.5	Squalls
10.06.2022	Thu	12	5	SW	1	
10.06.2022	Thu	18	4-5	SW-W	1	
10.07.2022	Fri	0	5	SW-W	1	
10.07.2022	Fri	6	5	SW	1	
10.07.2022	Fri	12	4-5	S-SW	0.5	
10.07.2022	Fri	18	4-5	S-SW	0.5	
10.08.2022	Sat	0	5	SW	1	Squalls
10.08.2022	Sat	6	5	SW-W	1	Rain
10.08.2022	Sat	12	4-5	W	0.5	Squalls
10.08.2022	Sat	18	5	W-NW	1	
10.09.2022	Sun	0	4	W	0.5	
10.09.2022	Sun	6	3-4	W	0.5	
10.09.2022	Sun	12	3-4	SW	0.5	
10.09.2022	Sun	18	3-4	SE-S	0	
10.10.2022	Mon	0	4-5	SE-S	0.5	
10.10.2022	Mon	6	4-5	SE-S	0.5	
10.10.2022	Mon	12	3-4	S-SW	0.5	
10.10.2022	Mon	18	5	SW-W	0.5	Rain
10.11.2022	Tue	0	5	W-NW	1	
10.11.2022	Tue	6	4-5	W	0.5	
10.11.2022	Tue	12	4	W-NW	0.5	
10.11.2022	Tue	18	4	W-NW	0.5	
10.12.2022	Wed	0	3	W-NW	0.5	
10.12.2022	Wed	6	2-3	W-NW	0	
10.12.2022	Wed	12	2-3	SW	0	
10.12.2022	Wed	18	2-3	S-SW	0	
10.13.2022	Thu	0	3-4	S	0.5	
10.13.2022	Thu	6	4	SE-S	0.5	
10.13.2022	Thu	12	3-4	S-SW	0.5	
10.13.2022	Thu	18	3-4	SW	0.5	
10.14.2022	Fri	0	3	S-SW	0.5	
10.14.2022	Fri	6	3-4	S-SW	0.5	
10.14.2022	Fri	12	3	S	0.5	
10.14.2022	Fri	18	2-3	S	0	
10.15.2022	Sat	0	3	S-SW	0.5	Rain
10.15.2022	Sat	6	2-3	SE-S	0	

Tab. 6.1   Ship's Meteorological Station

7   Station List

Station	MCS	Start Date	Start	Start Lati-	Start Longi-	End Date	End	End	End Longi-
AL582_3-1	001	10/6/2022	08:40	54°12.4	11°56.7	10/6/2022	15:09	54°02.3	11°07.8
AL582_3-1	002	10/6/2022	15:24	54°02.9	11°08.0	10/6/2022	21:51	54°13.2	11°56.5
AL582_3-1	003	10/6/2022	22:09	54°14.1	11°56.2	10/72022	04:21	54°03.5	11°07.9
AL582_3-1	004	10/7/2022	04:35	54°04.3	11°08.1	10/7/2022	10:46	54°04.8	11°56.4
AL582_3-1	005	10/7/2022	14:15	54°15.5	11°55.9	10/7/2022	21:30	54°04.8	11°08.0
AL582_3-1	006	10/7/2022	21:45	54°05.5	11°01.2	10/8/2022	02:16	54°11.3	11°39.9
AL582_3-1	007	10/8/2022	02:24	54°11.6	11°39.8	10/8/2022	06:50	54°06.3	11°08.0
AL582_3-1	008	10/8/2022	07:40	54°07.2	11°09.1	10/8/2022	13:39	54°16.3	11°55.9
AL582_3-1	009	10/8/2022	13:52	54°17.1	11°55.6	10/8/2022	17:57	54°09.6	11°22.0
AL582_3-1	010	10/8/2022	18:27	54°11.1	11°23.6	10/8/2022	22:38	54°17.8	11°55.6
AL582_3-1	011	10/8/2022	22:46	54°18.5	11°55.3	10/9/2022	02:13	54°12.6	11°24.9
AL582_3-1	012	10/9/2022	02:46	54°14.2	11°26.6	10/9/2022	06:26	54°19.1	11°55.2
AL582_3-1	013	10/9/2022	06:40	54°19.7	11°54.9	10/9/2022	10:09	54°15.7	11°27.8
AL582_3-1	014	10/9/2022	10:37	54°17.3	11°28.3	10/9/2022	13:43	54°20.2	11°55.1
AL582_3-1	015	10/9/2022	13:56	54°20.7	11°54.6	10/9/2022	16:59	54°18.9	11°28.6
AL582_3-1	016	10/9/2022	17:23	54°20.2	11°29.2	10/9/2022	20:19	54°21.0	11°54.7
AL582_3-1	017	10/9/2022	20:46	54°21.5	11°53.7	10/9/2022	23:08	54°10.1	11°47.1
AL582_3-1	018	10/9/2022	23:08	54°10.1	11°47.1	10/9/2022	23:51	54°10.8	11°41.4
AL582_3-1	019	10/9/2022	23:51	54°10.8	11°41.4	10/10/2022	02:08	54°20.6	11°31.1
AL582_3-1	020	10/10/2022	02:20	54°20.5	11°30.0	10/10/2022	05:30	54°04.7	11°24.3
AL582_3-1	021	10/10/2022	05:53	54°05.1	11°26.6	10/10/2022	07:30	54°13.0	11°30.7
AL582_3-1	022	10/10/2022	07:56	54°13.9	11°31.9	10/10/2022	09:28	54°16.4	11°44.6
AL582_3-1	023	10.10.2022	09:53	54°16.3	11°43.8	10.10.2022	11:40	54°13.9	11°31.8
AL582_3-1	024	10.10.2022	12:26	54°13.9	11°31.9	10.10.2022	14:15	54°16.8	11°46.7
AL582_5-1	032	11.10.2022	06:25	54°50.2	13°20.8	11.10.2022	08:08	54°41.8	13°23.7
AL582_5-1	033	11.10.2022	08:08	54°41.8	13°23.7	11.10.2022	09:44	54°36.3	13°24.3
AL582_5-1	034	11.10.2022	10:04	54°35.8	13°26.7	11.10.2022	10:46	54°39.2	13°27.5
AL582_5-1	035	11.10.2022	10:58	54°39.2	13°28.1	11.10.2022	11:41	54°15.5	13°27.4
AL582_5-1	036	11.10.2022	11:48	54°53.3	13°28.2	11.10.2022	13:14	54°42.5	13°30.2
AL582_5-1	037	11.10.2022	13:28	54°32.2	13°31.0	11.10.2022	14:53	54°35.0	13°29.0
AL582_5-1	038	11.10.2022	14:59	54°35.0	13°29.7	11.10.2022	16:30	54°42.2	13°32.3
AL582_5-1	039	11.10.2022	16:45	54°42.1	13°32.8	11.10.2022	18:10	54°35.1	13°30.5
AL582_5-1	040	11.10.2022	18:21	54°35.1	13°31.8	11.10.2022	19:46	54°42.0	13°34.2
AL582_5-1	041	11.10.2022	20:03	54°41.6	13°35.2	11.10.2022	21:23	54°35.2	13°33.3
AL582_5-1	042	11.10.2022	21:34	54°35.5	13°34.5	11.10.2022	10:51	54°41.7	13°15.7
AL582_5-1	043	11.10.2022	23:07	54°41.4	13°63.9	12.10.2022	00:18	54°35.6	13°36.7
AL582_5-1	044	12.10.2022	00:25	54°35.8	13°37.0	12.10.2022	01:42	54°42.3	13°38.5
AL582_5-1	045	12.10.2022	02:03	54°42.1	13°40.3	12.10.2022	03:28	54°35.2	13°39.9
AL582_5-1	046	12.10.2022	03:38	54°34.9	13°40.6	12.10.2022	05:02	54°42.0	13°42.6
AL582_5-1	047	12.10.2022	04:16	54°41.5	13°43.8	12.10.2022	06:38	54°34.9	13°40.9
AL582_5-1	048	12.10.2022	06:49	54°34.8	13°41.3	12.10.2022	08:12	54°41.5	13°44.3
AL582_5-1	049	12.10.2022	08:23	54°41.1	13°44.6	12.10.2022	09:08	54°37.5	13°42.7
AL582_5-1	050	12.10.2022	09:23	54°37.4	13°43.0	12.10.2022	10:10	54°41.1	13°45.0
AL582_5-1	051	12.10.2022	10:21	54°40.8	13°45.5	12.10.2022	11:40	54°34.7	13°41.5
AL582_5-1	052	12.10.2022	11:48	54° 34.4	13° 41.9	12.10.2022	13:08	54°40.1	13°47.7
AL582_5-1	053	12.10.2022	13:23	54°39.2	13°48.1	12.10.2022	14:38	54°34.1	13°42.0
AL582_5-1	054	12.10.2022	14:46	54°33.8	13°42.5	12.10.2022	15:42	54°36.9	13°48.1
AL582_5-1	055	12.10.2022	15:59	54°36.2	13°49.0	12.10.2022	16:58	54°33.1	13°42.2
AL582_5-1	056	12.10.2022	17:06	54°32.9	13°42.4	12.10.2022	17:50	54°34.9	13°47.76
AL582_5-1	057	12.10.2022	18:20	54°33.7	13°46.8	12.10.2022	21:10	54°38.4	13°27.1
AL582_5-1	058	12.10.2022	21:44	54°40.5	13°29.1	12.10.2022	23:41	54° 39.2	13°45.5
AL582_5-1	059	12.10.2022	23:59	54°39.1	13°45.0	13.10.2022	00:50	54°35.0	13°42.1
AL582_5-1	060	13.10.2022	00:50	54°35.0	13°42.1	13.10.2022	01:21	54°23.5	13°43.1
AL582_5-1	061	13.10.2022	01:21	54°23.5	13°43.1	13.10.2022	02:57	54°24.5	13°42.6
AL582_5-1	062	13.10.2022	03:04	54°24.3	13°43.5	13.10.2022	04:35	54°28.2	13°53.9
AL582_5-1	063	13.10.2022	04:50	54°27.3	13°54.5	13.10.2022	06:19	54°22.1	13°45.4
AL582_5-1	064	13.10.2022	06:40	54°21.1	13°47.1	13.10.2022	07:32	54°24.2	13°52.0
AL582_5-1	065	13.10.2022	07:45	54°23.6	13°52.3	13.10.2022	08:41	54°19.3	13°48.7
AL582_5-1	066	13.10.2022	08:58	54°18.4	13°48.9	13.10.2022	11:05	54°27.4	13°49.2

AL582_5-1	067	13.10.2022	11:24	54°26.6	13°59.9	13.10.2022	13:25	54°17.7	13°50.9
AL582_5-1	068	13.10.2022	13:41	54°17.5	13°52.7	13.10.2022	14:50	54°22.2	13°58.4
AL582_5-1	069	13.10.2022	15:02	54°21.5	13°59.1	13.10.2022	16:00	54°17.3	13°54.8
AL582_5-1	070	13.10.2022	16:17	54°17.4	13°57.1	13.10.2022	17:42	54°22.9	14°05.3
AL582_5-1	071	13.10.2022	18:03	54°21.5	14°06.5	13.10.2022	19:40	54°14.7	13°58.6
AL582_5-1	072	13.10.2022	20:08	54°12.8	13°58.9	13.10.2022	22:01	54°19.7	14°10.7
AL582_5-1	073	13.10.2022	22:14	54°90.1	14°11.2	13.10.2022	01:02	54°07.1	13°58.5
AL582_5-1	074	14.10.2022	01:13	54°06.7	13°59.4	14.10.2022	03:54	54°17.4	14°14.6
AL582_5-1	075	14.10.2022	04:07	54°16.8	14°15.3	14.10.2022	07:01	54°04.3	14°02.4
AL582_5-1	076	14.10.2022	07:24	54°03.4	14°04.8	14.10.2022	10:45	54°14.4	14°25.1

Tab. 7   Stationlist

8   Data and Sample Storage and Availability

(C. Hübscher)

Data measured on the short magnetics profiles can be made available at any time. However, they are internship data without any further use and will therefore not be archived for the long term. A national facility for long-term storing of seismic raw data is currently under development in the course of a NFDI4Earth project. Until then, data are stored at the University of Hamburg.

The moratorium for raw seismic and SES data ends September 1, 2023. Those data that will be processed in the course of qualification theses and publications will be made available upon completion of the qualification theses and resulting publications, but latest September 2024. Data will be provided upon reasonable request. This applies not to all data, since the processing of all data has been carried out on an undergraduate level with limited quality assurance.

The contact person is Christian Hübscher (Christian.huebscher@uni-hamburg.de)

Data Type	Database	Available	Open Access	Contact Peron:
Magnetic	local hard drives	immediately	immediately	C. Hübscher
SES raw	local hard drives	Sept. 2023	Sept. 2023	C. Hübscher
MCS raw	local hard drives	Sept. 2023	Sept. 2023	C. Hübscher
MCS processed	local hard drives	Sept. 2024	Sept. 2024	C. Hübscher

Tab. 8   Data availabilities

9   Acknowledgements

(C. Hübscher)

We like to thank Captain Tino Kaufmann and the professional crew of the RV ALKOR for their enthusiastic support during the entire cruise that enabled us to successfully complete our working program in a good atmosphere on board.

10   References

Ahlrichs, N., Hübscher, C., Noack, V., Schnabel, M., Damm, V., & Krawczyk, C. M., 2020. Structural evolution at the northeast North German Basin margin: From initial Triassic salt movement to Late Cretaceous-Cenozoic remobilization. Tectonics, 39(7), e2019TC005927.

Ahlrichs, N., Noack, V., Hübscher, C., Seidel, E., Warwel, A., & Kley, J., 2022. Impact of Late Cretaceous inversion and Cenozoic extension on salt structure growth in the Baltic sector of the North German Basin. Basin Research, 34(1), 220-250.

Al Hseinat, M., & Hübscher, C., 2017. Late Cretaceous to recent tectonic evolution of the North German Basin and the transition zone to the Baltic Shield/southwest Baltic Sea. Tectonophysics, 708, 28-55.

Al Hseinat, M., Hübscher, C., Lang, J., Lüdmann, T., Ott, I., & Polom, U., 2016. Triassic to recent tectonic evolution of a crestal collapse graben above a salt-cored anticline in the Glückstadt Graben/North German Basin. Tectonophysics, 680, 50-66.

Bachmann, G. H., and Hoffmann, N., 1997, Development of the Rotliegend basin in northern Germany, Geologisches Jahrbuch D103, 9-31..

Bachmann, G. H., Geluk, M. C., Doornenbal, J. C., & Stevenson, A. G., 2010. Petroleum geological atlas of the Southern Permian Basin area.

Bachmann, G. H., Voigt, T., Bayer, U., von Eynatten, H., Legler, B., & Littke, R., 2008. Depositional history and sedimentary cycles in the Central European Basin System. In Dynamics of Complex Intracontinental Basins: the Example of the Central European Basin System. Springer. pp. 156-172.

Bayer, U., Scheck, M., & Köhler, M., 1997. Modeling of the 3D thermal field in the northeast German basin. Geologische Rundschau, 86(2), 241-251.

Brink, H. J., Dürschner, H., & Trappe, H., 1992. Some aspects of the late and post-Variscan development of the Northwestern German Basin. Tectonophysics, 207(1-2), 65-95.

Dadlez, R., Marek, S., & Pokorski, J., 1998 . Paleogeographic atlas of epicontinental Permian and Mesozoic in Poland (1: 2 500 000). Polish Geological Institute, Warszawa.#

Dadlez, R., Narkiewicz, M., Stephenson, R. A., Visser, M. T. M., & Van Wees, J. D., 1995. Tectonic evolution of the Mid-Polish Trough: modelling implications and significance for central European geology. Tectonophysics, 252(1-4), 179-195.

Grassmann, S., Cramer, B., Delisle, G., Messner, J., & Winsemann, J., 2005. Geological history and petroleum system of the Mittelplate oil field, Northern Germany. International Journal of Earth Sciences, 94(5), 979-989.

Graversen, O., 2006. The Jurassic-Cretaceous North Sea rift dome and associated basin evolution. Search and discovery article, 30040.

Gupta, S., Cowie, P. A., Dawers, N. H., & Underhill, J. R., 1998. A mechanism to explain rift-basin subsidence and stratigraphic patterns through fault-array evolution. Geology, 26(7), 595-598.

Hansen, M. B., Scheck-Wenderoth, M., Hübscher, C., Lykke-Andersen, H., Dehghani, A., Hell, B., & Gajewski, D., 2007. Basin evolution of the northern part of the Northeast German Basin— Insights from a 3D structural model. Tectonophysics, 437(1-4), 1-16.

Herwanger, J. V., Schiøtt, C. R., Frederiksen, R., If, F., Vejbæk, O. V., Wold, R., ... & Koutsabeloulis, N., 2010. Applying time-lapse seismic methods to reservoir management and field development planning at South Arne, Danish North Sea. In Geological Society, London, Petroleum Geology Conference series (Vol. 7, No. 1, pp. 523-535). London: The Geological Society of London.

Hindenberg, K., 2000. Genese, Migration und Akkumulation von Erdöl in Mutter-und Speichergesteinen des Staßfurt Karbonat (Ca2) von Mecklenburg--Vorpommern und Südost-Brandenburg (No. PreJuSER-62745). Erdöl und Geochemie.

Hinsch, W., 1986. Lithologie, Stratigraphie und Paläogeographie des Paläogens in Schleswig-Holstein. Beiträge zur regionalen Geologie der Erde, 18, 10-21.

Hrvoic D., 2007. SeaSPY Overhauser Magnetometer Technical Application Guide. Underwater Hydroacoustics, Innomar SES 2000 light. (https://www.innomar.com/applicationvery-shallow-water.php, Retrieved October 8th, 2021)

Hübscher, C., Hansen, M. B., Trinanes, S. P., Lykke-Andersen, H., & Gajewski, D., 2010. Structure and evolution of the Northeastern German Basin and its transition onto the Baltic Shield. Marine and petroleum geology, 27(4), 923-938.

Hübscher, C., Hseinat, M. A. A., Schneider, M., & Betzler, C., 2019. Evolution of contourite systems in the late Cretaceous Chalk Sea along the Tornquist Zone. Sedimentology, 66(4), 1341-1360.

James, D., 2003. EVANS, D., GRAHAM, C., ARMOUR, A. & BATHURST, P.(editors and compilers) 2003. The Millennium Atlas: Petroleum Geology of the Central and Northern North Sea. 389 pp. London, Bath: Geological Society of London.

Japsen, P., Green, P. F., Nielsen, L. H., Rasmussen, E. S., & Bidstrup, T., 2007. Mesozoic–Cenozoic exhumation events in the eastern North Sea Basin: a multi-disciplinary study based on palaeothermal, palaeoburial, stratigraphic and seismic data. Basin Research, 19(4), 451-490.

Kammann, J., Hübscher, C., Boldreel, L. O., & Nielsen, L., 2016. High-resolution shear-wave seismics across the Carlsberg Fault zone south of Copenhagen—Implications for linking Mesozoic and late Pleistocene structures. Tectonophysics, 682, 56-64.

Katzung, G., 2004. Geologie von Mecklenburg-Vorpommern.

Kenzler, M., & Hüneke, H., 2019. Sea cliff at Glowe: stratigraphy and absolute age chronology of the Jasmund Pleistocene sedimentary record. DEUQUA special publications, 2, 43-50.

Kiersnowski, H., Paul, J., Peryt, T. M., & Smith, D. B., 1995. Facies, paleogeography, and sedimentary history of the Southern Permian Basin in Europe. In The Permian of Northern Pangea (pp. 119-136). Springer, Berlin, Heidelberg.

Kley, J., & Voigt, T., 2008. Late Cretaceous intraplate thrusting in central Europe: Effect of Africa-Iberia-Europe convergence, not Alpine collision. Geology, 36(11), 839-842.

Kley, J., 2018. Timing and spatial patterns of Cretaceous and Cenozoic inversion in the Southern Permian Basin. Geological Society, London, Special Publications, 469(1), 19-31.

Kossow, D., & Krawczyk, C. M., 2002. Structure and quantification of processes controlling the evolution of the inverted NE-German Basin. Marine and Petroleum Geology, 19(5), 601-618.

Kossow, D., & Krawczyk, C. M., 2002. Structure and quantification of processes controlling the evolution of the inverted NE-German Basin. Marine and Petroleum Geology, 19(5), 601-618.

Kossow, D., Krawczyk, C., McCann, T., Strecker, M., & Negendank, J. F., 2000. Style and evolution of salt pillows and related structures in the northern part of the Northeast German Basin. International Journal of earth sciences, 89(3), 652-664.

Krawczyk, C. M., Stiller, M., & DEKORP–BASIN Research Group., 1999. Reflection seismic constraints on Paleozoic crustal structure and Moho beneath the NE German Basin. Tectonophysics, 314(1-3), 241-253.

Littke, R., Bayer, U., Gajewski, D., & Nelskamp, S. (Eds.)., 2008. Dynamics of complex intracontinental basins: the central European basin system. Springer Science & Business Media.

Littke, R., Scheck-Wenderoth, M., Brix, M. R., & Nelskamp, S., 2008. Subsidence, inversion and evolution of the thermal field. In Dynamics of complex intracontinental basins: the Central European Basin System (pp. 125-153). Springer.

Lokhorst, A., 1998. The Northwest European Gas Atlas. NITG-TNO, Haarlem, The Netherlands.

Magri, F., Littke, R., Rodon, S., & Urai, J. L., 2008. Temperature fields, petroleum maturation and fluid flow in the vicinity of salt domes. In Dynamics of Complex Intracontinental Basins: The Central European Basin System (pp. 323-344). Springer.

Marotta, A. M., Bayer, U., & Thybo, H., 2000. The legacy of the NE German Basin—reactivation by compressional buckling. Terra Nova, 12(3), 132-140.

Maystrenko, Y., Bayer, U., & Scheck-Wenderoth, M., 2005. Structure and evolution of the Glueckstadt Graben due to salt movements. International Journal of Earth Sciences, 94(5), 799-814.

Maystrenko, Y., Bayer, U., & Scheck-Wenderoth, M., 2006. 3D reconstruction of salt movements within the deepest post-Permian structure of the Central European Basin System-the Glueckstadt Graben. Netherlands Journal of Geosciences, 85(3), 181-196.

Maystrenko, Y., Bayer, U., Brink, H. J., & Littke, R., 2008. The Central European basin system–an overview. Dynamics of complex intracontinental basins, 16-34.

McCann, T., 1999. The tectonosedimentary evolution of the northern margin of the Carboniferous foreland basin of NE Germany. Tectonophysics, 313(1-2), 119-144.

Nielsen, S. B., Paulsen, G. E., Hansen, D. L., Gemmer, L., Clausen, O. R., Jacobsen, B. H., ... & Gallagher, K., 2002. Paleocene initiation of Cenozoic uplift in Norway. Geological Society, London, Special Publications, 196(1), 45-65.

Plein, E., 1995. Stratigraphie von Deutschland I–Norddeutsches Rotliegendbecken, Rotliegend-Monographie Teil II, Courier Forschungsinst. Senckenberg, Frankfurt a. M, S, 183, 193.

Rodon, S., & Littke, R., 2005. Thermal maturity in the Central European Basin system (Schleswig-Holstein area): results of 1D basin modelling and new maturity maps. International Journal of Earth Sciences, 94(5), 815-833.

Scheck, M., Barrio-Alvers, L., Bayer, U., & Götze, H. J., 1999. Density structure of the Northeast German Basin: 3D modelling along the DEKORP line BASIN96. Physics and Chemistry of the Earth, Part A: Solid Earth and Geodesy, 24(3), 221-230.

Scheck-Wenderoth, M., & Lamarche, J., 2005. Crustal memory and basin evolution in the Central European Basin System—new insights from a 3D structural model. Tectonophysics, 397(1-2), 143-165.

Schretzenmyar, S., 1993. Bruchkinematik des Haldenslebener und Gardelegener Abbruchs (Scholle von Calvörde). Geologisches Jahrbuch. Reihe A, Allgemeine und regionale Geologie BR Deutschland und Nachbargebiete, Tektonik, Stratigraphie, Paläontologie, 1993(131), 219-238.

Steffen, R., Wu, P., & Lund, B., 2021. Geomechanics of Glacially-Triggered Faulting. H. Steffen, O. Olesen & R. Sutinen, Cambridge University Press, Cambridge, UK.

Strohmenger, C., Voigt, E., & Zimdars, J., 1996. Sequence stratigraphy and cyclic development of Basal Zechstein carbonate-evaporite deposits with emphasis on Zechstein 2 off-platform carbonates (Upper Permian, Northeast Germany). Sedimentary Geology, 102(1-2), 33-54.

Underhill, J. R., & Partington, M. A., 1993. Jurassic thermal doming and deflation in the North Sea: implications of the sequence stratigraphic evidence. In Geological Society, London, Petroleum Geology Conference Series (Vol. 4, No. 1, pp. 337-345). Geological Society of London.

Van Wees, J. D., Stephenson, R. A., Ziegler, P. A., Bayer, U., McCann, T., Dadlez, R., ... & Scheck, M., 2000. On the origin of the southern Permian Basin, Central Europe. Marine and Petroleum Geology, 17(1), 43-59.

Vejbæk, O. V., 1997. Dybe strukturer i danske sedimentære bassiner. Dansk Geologisk Forening.

Vejbæk, O. V., Andersen, C., Dusar, M., Herngreen, G. F. W., Krabbe, H., Leszczyński, K., ... & Van der Molen, A. S., 2010. Cretaceous. Petroleum geological atlas of the southern Permian Basin Area, 195-209.

Vinken, R., 1988. The Northwest European Tertiary Basin:-results of the International Geological Correlation-Programme, Project No. 124.

Walaszczyk, I., Wood, C. J., Lees, J. A., Peryt, D., Voigt, S., & Wiese, F. (2010). The Salzgitter-Salder quarry (Lower Saxony, Germany) and Słupia Nadbrzeżna river cliff section (Central Poland): a proposed candidate composite global boundary stratotype section and point for the Coniacian stage (upper Cretaceous). Acta Geologica Polonica, 60(4), 445-477.

Warsitzka, M., Jähne-Klingberg, F., Kley, J., & Kukowski, N., 2019. The timing of salt structure growth in the Southern Permian Basin (Central Europe) and implications for basin dynamics. Basin Research, 31(2), 337-360.

Wunderlich, J., & Wendt, G., 2001. Advantages of parametric acoustics for the detection of the dredging level in areas with siltation. In Proc. of the 7th Workshop on Dredging and Surveying, Scheveningen. pp. 67-75.

Ziegler, P. A.,1990. Geological Atlas of Western and Central Europe. 2nd edn, Shell Internationale Petroleum Maatschappij, The Hague. In Geological Society, London.

11   Abbreviations

CMP	Common Mid Point
CSP	Capacitor Sparker Power Unit
G.I	Generator Injector
GPS	Global Positioning System
HPAC	High Pressure Air Compressor
ISO	International Organization for Standardization
MBES	Multibeam Echosounder
MRU	Motion Reference Unit
RMS	Root Mean Square
SEG-Y	Data format, Society of Exploration Geophysicists
SES	Sediment Echo Sounder
SESWIN	Processing Software, SES for Windows
Sig.	Significant wave height
SIS	Seafloor Information System
UTC	Universal Time Coordinated
UTM	Universal Transverse Mercator
NGB	North German basin
SPB	Southern Permian Basin